

THE AGN, STAR-FORMING, AND MORPHOLOGICAL PROPERTIES OF LUMINOUS IR-BRIGHT/OPTICALLY-FAINT GALAXIES

J. L. DONLEY^{1,2,5}, G. H. RIEKE², D. M. ALEXANDER³, E. EGAMI², AND P. G. PÉREZ-GONZÁLEZ^{2,4}

¹ Space Telescope Science Institute, 3700 San Martin Drive, Baltimore, MD 21218, USA; donley@stsci.edu

² Steward Observatory, University of Arizona, 933 North Cherry Avenue, Tucson, AZ 85721, USA

³ Department of Physics, Durham University, Durham DH1 3LE, UK

⁴ Departamento de Astrofísica y CC. de la Atmósfera, Facultad de CC. Físicas, Universidad Complutense de Madrid, 28040 Madrid, Spain

Received 2009 December 14; accepted 2010 June 10; published 2010 July 29

ABSTRACT

We present the active galactic nucleus (AGN), star-forming, and morphological properties of a sample of 13 MIR-luminous ($f_{24} \gtrsim 700 \mu\text{Jy}$) IR-bright/optically-faint galaxies (IRBGs, $f_{24}/f_R \gtrsim 1000$). While these $z \sim 2$ sources were drawn from deep *Chandra* fields with >200 ks X-ray coverage, only seven are formally detected in the X-ray and four lack X-ray emission at even the 2σ level. *Spitzer* InfraRed Spectrograph (IRS) spectra, however, confirm that all of the sources are AGN-dominated in the mid-IR, although half have detectable polycyclic aromatic hydrocarbon (PAH) emission responsible for $\sim 25\%$ of their mid-infrared flux density. When combined with other samples, this indicates that at least 30%–40% of luminous IRBGs have star formation rates in the ultraluminous infrared galaxy (ULIRG) range (~ 100 – $2000 M_{\odot} \text{ yr}^{-1}$). X-ray hardness ratios and MIR to X-ray luminosity ratios indicate that all members of the sample contain heavily X-ray obscured AGNs, 80% of which are candidates to be Compton thick. Furthermore, the mean X-ray luminosity of the sample, $\log L_{2-10 \text{ keV}} (\text{erg s}^{-1}) \sim 44.6$, indicates that these IRBGs are Type 2 QSOs, at least from the X-ray perspective. While those sources most heavily obscured in the X-ray are also those most likely to display strong silicate absorption in the mid-IR, silicate absorption does not always accompany X-ray obscuration. Finally, $\sim 70\%$ of the IRBGs are merger candidates, a rate consistent with that of sub-mm galaxies (SMGs), although SMGs appear to be physically larger than IRBGs. These characteristics are consistent with the proposal that these objects represent a later, AGN-dominated, and more relaxed evolutionary stage following soon after the star-formation-dominated one represented by the SMGs.

Key words: galaxies: active – infrared: galaxies – X-rays: galaxies

Online-only material: color figures

1. INTRODUCTION

Studies of heavily obscured star-forming galaxies and active galactic nuclei (AGNs) in the distant universe have lagged behind those of their unobscured counterparts, largely due to their extreme faintness in the optical and UV. This optical faintness, however, need not be a limitation and can instead be used as a selection criterion, as dust-enshrouded sources faint at short wavelengths should be comparably bright in the infrared where their absorbed radiation is re-emitted. One might therefore expect sources with bright infrared emission yet faint optical fluxes ($f_{24}/f_R \gtrsim 1000$) to be ideal obscured galaxy/AGN candidates, and indeed, such sources comprised some of the first *Spitzer Space Telescope* (Werner et al. 2004) targets.

Initial studies of the brightest ($f_{24} \gtrsim 700 \mu\text{Jy}$) IR-bright/optically-faint galaxies (referred to here as IRBGs) targeted for *Spitzer* InfraRed Spectrograph (IRS; Houck et al. 2004) mid-infrared spectroscopic follow-up observations indicated that most lie at $z \sim 2$ and have either featureless spectra or spectra dominated by silicate absorption, properties indicative of AGN activity (e.g., Houck et al. 2005; Yan et al. 2005; Weedman et al. 2006a). Their optical faintness was therefore attributed both to distance as well as to obscuration by the dust surrounding an AGN’s central engine, although more recent studies suggest that the AGN’s host galaxy may also contribute significantly to the observed extinction (Brand et al. 2007; Polletta et al. 2008).

Subsequent multi-wavelength studies have since confirmed the AGN nature of the most luminous IRBGs, although they

reach differing conclusions concerning the relative importance of star formation and AGN activity among fainter ($f_{24} < 700 \mu\text{Jy}$) IRBGs (e.g., Dey et al. 2008; Donley et al. 2008; Georgantopoulos et al. 2008; Fiore et al. 2008; Pope et al. 2008a; Desai et al. 2009; Treister et al. 2009; Fiore et al. 2009; Georgakakis et al. 2010). Furthermore, they have shown that the space density of the most luminous IRBGs is comparable to that of luminous, unobscured AGNs at $z = 2$ (Dey et al. 2008). If these sources are in fact heavily obscured AGNs, they therefore represent an important phase in the growth of supermassive black holes during the era in which both star formation and AGN activity peaked.

To constrain the level of obscuration in these luminous AGNs, studies turned to the X-ray. Unfortunately, the large-area survey fields from which the luminous, and therefore rare, IRBGs were initially selected (e.g., the *Spitzer* First-Look Survey, the NOAO Deep Wide Field Survey, and the SWIRE Survey) and then followed-up with IRS have minimal X-ray coverage capable of detecting only the brightest AGN (Dey et al. 2008). Nonetheless, studies in these fields suggest that at least $\sim 50\%$ and perhaps as many as 95% of X-ray-detected IRBGs with $f_{24} > 1.3 \text{ mJy}$ are X-ray-obscured AGNs (Lanzuisi et al. 2009), some of which may be Compton thick (Polletta et al. 2006; Alexander et al. 2008b).

Alternatively, other studies have focused on samples of IRBGs selected in fields with deeper X-ray coverage, such as the *Chandra* Deep Fields and COSMOS. The deepest X-ray fields, however, are also the smallest, so those studies most suited to constrain X-ray obscuration are also those in which the focus generally shifts to the fainter and more numerous

⁵ Giacconi Fellow.

population of IRBGs whose nature remains controversial. In the larger COSMOS field, however, Fiore et al. (2009) find that 40% of IRBGs with moderate flux densities of $f_{24} > 550 \mu\text{Jy}$ are detected in the X-ray with a mean rest-frame obscured luminosity of $\log L_{2-10\text{keV}}(\text{erg s}^{-1}) = 43.5$ and an X-ray hardness ratio ($\text{HR} = (H - S)/(H + S)$, where $H = 1.5\text{--}6 \text{ keV}$ and $S = 0.3\text{--}1.5 \text{ keV}$) of 0.50, consistent with obscured yet Compton-thin absorption. The stacked X-ray signal from the remaining 60% of the sample has a similar HR of 0.53, although its interpretation is dependent on a number of factors including the assumed underlying column density distribution, the intrinsic MIR/X-ray luminosity ratio, and most importantly, the assumed photon index of emission from star formation. Assuming a star-forming X-ray photon index (Γ) of 1.9, Fiore et al. (2009) conclude that 94% of the X-ray non-detected, $f_{24} > 550 \mu\text{Jy}$ IRBGs are heavily obscured, and likely Compton thick, AGNs. If a harder X-ray photon index of $\Gamma \sim 1.0\text{--}1.4$ (as observed in the starburst-dominated ultraluminous infrared galaxies (ULIRGS) of Franceschini et al. 2003, Ptak et al. 2003, and Teng et al. 2005) is assumed, however, the obscured AGN fraction of this moderate-luminosity sample falls significantly.

To bridge the gap between these infrared and X-ray studies and therefore better constrain the luminosity, obscuration, and power sources of these cosmologically interesting AGNs, we have obtained IRS spectra of a sample of IRBGs selected in deep X-ray fields with effective exposures of $T_x > 200 \text{ ks}$. Because we do not require that our targets be *detected* in the X-ray, however, we do not bias our sample toward the brightest or least-obscured galaxies (e.g., Brand et al. 2008). The sample discussed below is therefore the first uniformly selected sample of IRBGs with both deep X-ray and IRS coverage. Because they were selected from deep multi-wavelength fields, many of the sources also have *Hubble Space Telescope* (HST) ACS imaging, enabling a morphological study of this unbiased sample and a comparison to sub-mm galaxies (SMGs), a population of $z \sim 2$ star-forming galaxies proposed by some to be the merger-induced progenitors of luminous IRBGs (e.g., Brodwin et al. 2008; Dey et al. 2008; Pope et al. 2008a; Coppin et al. 2010; Narayanan et al. 2010a, 2010b).

The paper is organized as follows. In Section 2, we discuss the sample selection, observations and data reduction. The optical and infrared photometric properties of the sources are then examined in Section 3. In Section 4, we present the IRS spectra and discuss the AGN and star-forming contribution to the MIR emission of these sources. The X-ray emission is discussed in Section 5, as is the agreement between the X-ray and IR properties, and the star formation rates (SFRs) of the sources are discussed in Section 6. In Section 7, we summarize the morphological properties of the IRBGs' hosts and compare them to those of the SMGs. The discussion follows in Section 8, and we then summarize our conclusions in Section 9. Throughout the paper, we assume the following cosmology: $(\Omega_m, \Omega_\Lambda, H_0) = (0.27, 0.73, 70.5 \text{ km s}^{-1} \text{ Mpc}^{-1})$, and quote all magnitudes in the AB system unless otherwise noted.

2. SAMPLE SELECTION AND OBSERVATIONS

To ensure deep X-ray coverage, we selected the IRBG sample from the Chandra Deep Fields North and South (CDF-N, CDF-S, $T_x \sim 2 \text{ Ms}$; Alexander et al. 2003; Luo et al. 2008), the Extended Chandra Deep Field South (E-CDFS, $T_x \sim 250 \text{ ks}$; Lehmer et al. 2005), and the Extended Groth Strip (EGS, $T_x \sim 200 \text{ ks}$; Laird et al. 2009), the combined area of which is 0.96 deg^2 . We chose for IRS follow-up sources with extreme

IR/optical flux ratios ($f_{24}/f_R \gtrsim 1000$) typical of those in Houck et al. (2005), Yan et al. (2005), and Weedman et al. (2006a, 2006b) based on the *Spitzer* MIPS $24 \mu\text{m}$ and optical photometry compiled in Pérez-González et al. (2008) and the UCM Extragalactic Database.⁶ In addition, we required flux densities in excess of $f_{24} \gtrsim 700 \mu\text{Jy}$ to guarantee that IRS spectra could be obtained in a reasonable amount of time. The final sample is comprised of 13 IRBGs.

The three sources in the CDF-N were observed with IRS as part of programs 20456 (PI: Chary) and 20733 (PI: Urry), and the spectra of two (IRBG5 and IRBG7) can be found in Pope et al. (2008b) and Murphy et al. (2009). For the remaining 10 sources, we obtained first and second order spectra with the IRS Long-Low (LL) module (program 30419, PI: Rieke). Observation details are given in Table 1. The resulting wavelength range of $14\text{--}37 \mu\text{m}$ guarantees coverage of the $9.7 \mu\text{m}$ silicate absorption feature at $z = 0.4\text{--}2.8$ and the $7.7 \mu\text{m}$ aromatic (hereafter polycyclic aromatic hydrocarbon (PAH)) feature at $z = 0.8\text{--}3.8$. Of the 13 sources in our sample, 4 have optical/NIR spectroscopic redshifts from the literature, placing them at $1.6 \leq z \leq 2.0$ (Szokoly et al. 2004; Swinbank et al. 2004; Davis et al. 2007).

2.1. Data Reduction

The IRS data were reduced using the *IrsLow* package developed by D. Fadda to accurately measure low-resolution spectra of faint, high redshift sources (see Fadda et al. 2010, for more details). Briefly, this package corrects for residual background, rogue pixels (pixels with high dark current and/or photon responsiveness), and cosmic rays, and takes into account all frames produced by the IRS/SSC pipeline. The background and noise images are produced by masking the target spectrum (and any serendipitous spectra) on each frame and then co-adding the resulting frames. A biweight statistical estimator is then used iteratively and interactively to minimize the contamination from deviant pixels, and pixels that deviate by more than 5σ from the mean local value are flagged as rogue. After rejecting any cosmic ray events and taking the spectral distortion into account, the spectra are then weighted by the point-spread function (PSF), optimally extracted, and co-added to produce the final spectrum.

3. OPTICAL/IR PHOTOMETRIC PROPERTIES

We list in Table 2 the optical and IR characteristics of the IRBGs. The 13 sources in our sample have $24 \mu\text{m}$ flux densities ranging from 701 to 2299 μJy (median $f_{24} = 1069 \mu\text{Jy}$), *R*-band magnitudes ranging from 23.7 to 25.3 AB (median $R = 24.8$ AB), and $24 \mu\text{m}$ to *R*-band flux ratios ranging from 1204 to 3961 (median $f_{24}/f_R = 2152$).

To place these sources in the context of recent studies, we also show in Table 3 the IR-excess selection criterion met by each of the 13 IRBGs. All sources meet the dust-obscured galaxy (DOG) criterion of Dey et al. (2008, $f_{24}/f_R \geq 1000$, $f_{24} > 0.3 \text{ mJy}$), and all but two meet one or more of the Houck et al. (2005, $f_{24} > 0.75 \text{ mJy}$, $R_{\text{Vega}} > 24.5$), Yan et al. (2005, $\log(vf_v(24 \mu\text{m})/vf_v(8 \mu\text{m})) \geq 0.5$, $\log(vf_v(24 \mu\text{m})/vf_v(0.7 \mu\text{m})) \geq 1.0$), or Weedman et al. (2006a, 2006b, $f_{24} > 1.0 \text{ mJy}$, $R_{\text{Vega}} > 23.9$) selection criteria. Furthermore, nine sources meet the IR-excess criteria of Fiore et al. (2008, $f_{24}/f_R \geq 1000$, $(R - K)_{\text{Vega}} \geq 4.5$) or Georgantopoulos et al. (2008, $f_{24}/f_R \geq 1000$, $R_{\text{AB}} - m_{3.6 \mu\text{m, AB}} > 3.7$), and eight meet the combined MIPS/IRAC criteria defined by

⁶ <http://guaix.fis.ucm.es/~pgperez/Proyectos/ucmcsdatabase.en.html>

Table 1
Observations

ID	Field	Program	Observation	Ramp Duration (s)		Number of Cycles		Total Integration (s) ^d
				LL1 ^b	LL2 ^c	LL1 ^b	LL2 ^c	
IRBG1	E-CDFS	30419	2006 Sept 15	120	120	10	10	4800
IRBG2	CDF-S	30419	2007 Aug 31	120	120	23	23	11040
IRBG3	E-CDFS	30419	2006 Sept 14	120	120	27	27	12960
IRBG4	CDF-S	30419	2007 Aug 31	120	120	15	15	7200
IRBG5	CDF-N	20456 ^e	2006 Apr 24	120	120	6	6	2880
IRBG6	CDF-N	20733	2006 May 26	30	30	80	80	12880
IRBG7	CDF-N	20456 ^f	2006 Apr 22	120	120	6	6	9600
IRBG8	EGS	30419	2007 Apr 27	120	120	12	12	5760
IRBG9	EGS	30419	2006 Jun 26	120	120	4	4	1920
IRBG10	EGS	30419	2007 Apr 27	120	120	7	7	3360
IRBG11	EGS	30419	2007 Mar 25	120	120	28	28	13440
IRBG12	EGS	30419	2007 Mar 25	120	120	18	18	8640
IRBG13	EGS	30419	2007 Apr 27	120	120	6	6	2880

Notes.

^a The PI's of programs 30419, 20456, and 20733 are G. H. Rieke, R. Chary, and C. M. Urry, respectively.

^b Long Low 1st order, 19.5–38.0 μm .

^c Long Low 2nd order, 14.0–21.3 μm .

^d The IRS nodding performed in Standard Staring mode results in two spectra per cycle, each with an exposure time equal to the ramp duration.

^e The IRS spectrum for this source was previously published in Pope et al. (2008b) and Murphy et al. (2009).

^f The IRS spectrum for this source was previously published in Murphy et al. (2009).

Table 2
IR-Bright/Optically-Faint Sample

ID	RA (J2000)	DECL. (J2000)	$z_{\text{spec}}^{\text{a}}$	$z_{\text{IRS}}^{\text{b}}$	f_{24} (μJy)	$R(\text{AB})$	f_{24}/f_{R}	$\alpha_{\text{IRAC}}^{\text{c}}$	$\alpha_{\text{IRS}}^{\text{c}}$	AGN% ^d	$f_{24,\text{SF}}^{\text{e}}$ (μJy)	$\tau_{9.7 \mu\text{m}}^{\text{f}}$	$L_6 \mu\text{m}^{\text{g}}$
IRBG1	03:31:46.6	-27:45:53.0	1069	25.3	3961	-1.92	-2.08	96 ± 2	41	0.0	45.6
IRBG2	03:31:58.3	-27:50:42.2	...	2.28 ± 0.06	851	25.2	2934	-1.86	-2.43	94 ± 5	99	0.5	45.6
IRBG3	03:32:10.5	-28:01:09.2	...	1.62 ± 0.02	751	25.1	2208	-1.46	-2.06	71 ± 4	286	0.4	45.0
IRBG4	03:32:37.8	-27:52:12.5	1.60	...	1066	24.8	2370	-1.78	-2.07	100 ± 3	0	0.0	45.2
IRBG5	12:36:00.2	62:10:47.3	2.00	2.00 ± 0.03	1144	24.0	1204	-2.13	-2.06	84 ± 3	293	0.1	45.4
IRBG6	12:36:35.6	62:14:23.9	2.02	2.04 ± 0.004	1497	23.8	1426	-2.00	-2.04	85 ± 1	351	0.0	45.6
IRBG7	12:37:26.5	62:20:27.0	...	1.76 ± 0.02	883	25.0	2324	-2.21	-1.81	$> 72^{\text{h}}$	272	5.2	45.4
IRBG8	14:15:38.1	52:18:52.9	1217	24.9	2967	...	-1.29	90 ± 6	122	0.1	45.7
IRBG9	14:16:35.4	52:12:35.2	2299	23.7	1999	-2.53	-1.92	92 ± 4	327	0.2	45.9
IRBG10	14:18:51.5	52:48:35.9	1.92	1.99 ± 0.02	1686	24.0	1812	...	-2.32	88 ± 3	394	0.3	45.6
IRBG11	14:20:08.6	53:01:10.1	...	2.07 ± 0.02	701	24.7	1491	...	-1.94	92 ± 9	57	5.0	45.5
IRBG12	14:20:13.0	52:55:33.3	...	1.04 ± 0.01	948	24.8	2106	...	-2.64	78 ± 3	218	0.1	44.3
IRBG13	14:20:21.9	52:55:12.1	...	2.60 ± 0.06	1786	24.1	2152	...	-0.58	79 ± 5	440	1.4	46.1

Notes.

^a Optical/NIR spectroscopic redshift from the literature.

^b IRS-derived redshift (this work); see Section 4.

^c IRAC (3.6–8.0 μm) and IRS (14–37 μm) power-law slopes, where $f_{\nu} \propto \nu^{\alpha}$.

^d AGN contribution to the MIR (14–37 μm) flux density.

^e Star-forming contribution to the observed 24 μm flux, as determined by the spectral fit.

^f Optical depth of best-fit AGN continuum at 9.7 μm (see Section 4).

^g Rest-frame 6 μm luminosity of the AGN component (see Section 5.2).

^h IRS spectrum not fit by default model. See Section 4.1 for details.

References. Spectroscopic redshifts from Szokoly et al. (2004, IRBG4), Swinbank et al. (2004, IRBG5, IRBG6), and Davis et al. (2007, IRBG10)

Polletta et al. (2008) to select highly luminous and heavily obscured AGNs.

3.1. SEDs

The broadband (0.4–70 μm) spectral energy distributions (SEDs) of the IRBGs are shown in Figure 1. We constructed the SEDs by first compiling aperture-matched photometric catalogs using the CDF-S data of Marzke et al. (1999, *RIz*), Vandame et al. (2001, *JK*), Arnouts et al. (2002, *UU_pBVRI*), COMBO17 (Wolf et al. 2004), Giavalisco et al. (2004, *bviziHK*), Le Fèvre et al. (2004, *I*), and GALEX (*FUV*, *NUV*), the CDF-N data of

Giavalisco et al. (2004, *bvizi*) and Capak et al. (2004, *UB-VRIz'HK'*), and the EGS data (*UBgVRIzJK*) of Villar et al. (2008) and Barro et al. (2010). For more details on the available data sets and the aperture-matching procedure, see Pérez-González et al. (2005, 2008) and the UCM Extragalactic Database (see footnote 6).

While a handful of the source SEDs shown in Figure 1 display a weak stellar bump (the broad 1.6 μm feature that dominates the SEDs of star-forming galaxies and which tends to be correlated with the presence of PAH emission in IRBGs (e.g., Desai et al. 2009)), the majority of the sources in our sample have power-

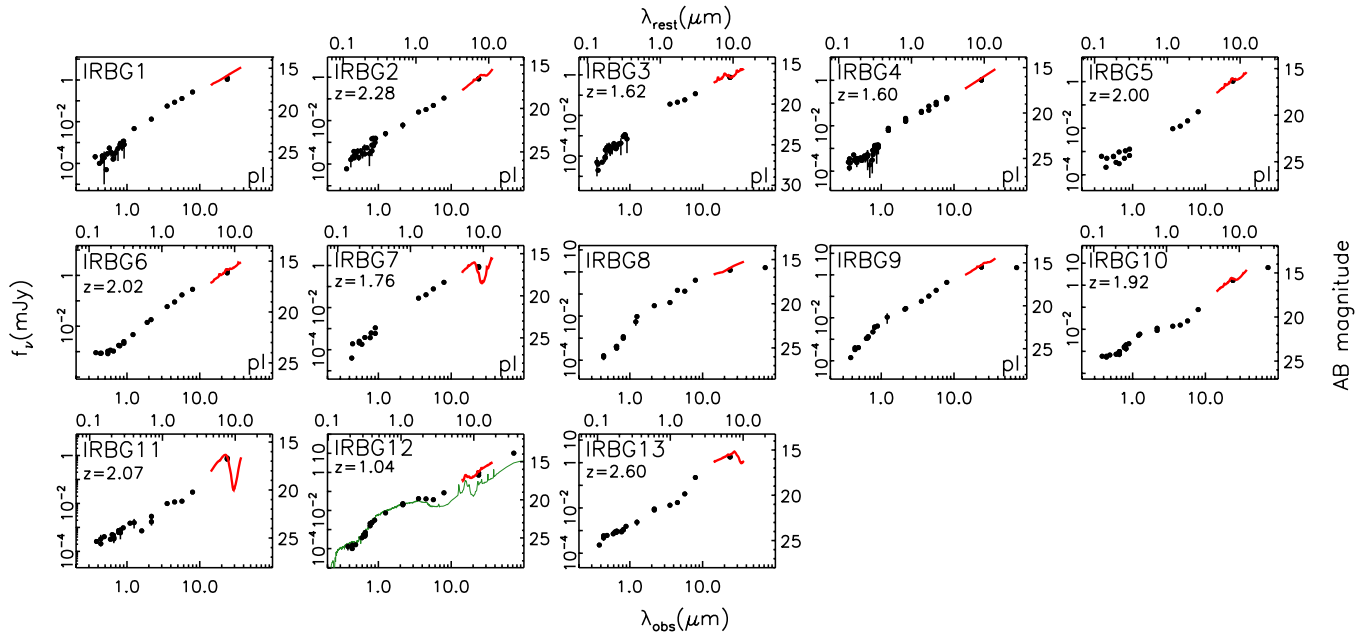


Figure 1. Broadband SEDs of the 13 IRBGs. The majority show power-law SEDs that extend from the near to mid-IR. Those sources that meet the formal IRAC power-law criterion (see Section 3.1) are indicated by a “pl” in the lower right corner. The best fits to the IRS spectra (see Section 4) are shown in solid (red) lines and the template of NGC 6090 is overplotted (in green) on the SED of IRBG12 to confirm its low redshift ($z \sim 1$; see Section 4.1).

(A color version of this figure is available in the online journal.)

Table 3
IR Selection Criteria

ID	H05	Y05	W06	D08	F08	G08	P08	L09	PL
IRBG1	x	...	x	x	x	x	x
IRBG2	x	x	x	x	x	...	x
IRBG3	x	x	—	x	x
IRBG4	x	...	x	x	x	x	x	...	x
IRBG5	...	x	...	x	—	...	x	...	x
IRBG6	x	x	x	x	...	x
IRBG7	x	x	—	x	x	...	x
IRBG8	x	...	x	x	x	x	x
IRBG9	x	x	x	x	...	x
IRBG10	...	x	...	x
IRBG11	...	x	...	x
IRBG12	x	x	...	x	x	x
IRBG13	x	x	x	x	...

Notes. An “x” indicates that a source would be selected via the listed criteria and a “—” indicates that a source lacked the necessary data to determine if it would be selected.

References. H05: Houck et al. (2005), Y05: Yan et al. (2005), W06: Weedman et al. (2006a, 2006b), D08: Dey et al. (2008) (DOGS), F08: Fiore et al. (2008), G08: Georgantopoulos et al. (2008), P08: Polletta et al. (2008), L09: Lanzuisi et al. (2009) (EDOGS), PL (power-law): Alonso-Herrero et al. (2006); Donley et al. (2007)

law SEDs indicative of AGN activity. When we apply the IRAC (3.6–8.0 μm) power-law selection criterion used by Alonso-Herrero et al. (2006) and Donley et al. (2007) to identify AGN-dominated sources, we find that 7 of the 13 sources are indeed power-law AGNs and one additional source (IRBG5) meets the criterion if we lower the required chi-squared probability from $P_\chi > 0.1$ to $P_\chi > 0.01$ (e.g., Alonso-Herrero et al. 2006).⁷ Because the IRAC photometry of IRBG8 is questionable due

to its position near the edge of the IRAC field, the total power-law fraction is $\sim 8/12$ or $\sim 70\%$. Our results are therefore in agreement with those of Dey et al. (2008), who find that while only $\sim 20\%$ of IRBGs at $f_{24} = 300 \mu\text{Jy}$ have power-law SEDs, the power-law fraction rises to $\sim 55\%$ at $f_{24} = 700 \mu\text{Jy}$ (our flux cut) and to $\sim 70\%$ – 85% at $f_{24} > 1000 \mu\text{Jy}$ (the median flux density of our sample). Furthermore, all of the power-law sources in our sample are extremely red, with a mean slope of $\alpha = -1.99$ (where $f_\nu \propto \nu^\alpha$), and are therefore strong AGN candidates regardless of redshift (see Donley et al. 2007, 2008).

3.2. Infrared Colors

A number of infrared color criteria have been used in the literature to discriminate between AGN and star formation activity (for a review, see Donley et al. 2008). While the reliability and completeness of pure color/color cuts is heavily dependent on a source’s redshift, Pope et al. (2008a) find that for IRBGs (which typically lie at $z \sim 2$), $f_{8.0 \mu\text{m}}/f_{4.5 \mu\text{m}} = 2.0$ provides a convenient dividing line between star-formation-dominated ($f_{8.0 \mu\text{m}}/f_{4.5 \mu\text{m}} < 2.0$) and AGN-dominated ($f_{8.0 \mu\text{m}}/f_{4.5 \mu\text{m}} > 2.0$) emission (also see Coppin et al. 2010, who suggest an even lower cut of 1.65). As a confirmation of this method, we plot in Figure 2 the expected colors of a number of AGN and star-forming galaxies. We find that only AGNs fall redward of the cut, as expected, although we note that lower-luminosity AGNs (e.g., Seyfert galaxies) as well as self-absorbed AGNs (Treister et al. 2009) could display bluer colors more typical of star-forming galaxies. As shown in Figure 2, however, all of our IRBGs lie in the red AGN-dominated regime, with three sources showing a significantly higher $f_{24 \mu\text{m}}/f_{8.0 \mu\text{m}}$ ratio than the rest. Pope et al. (2008a) attribute this excess of $24 \mu\text{m}$ emission either to intrinsic obscuration indicative of AGN activity, which enhances the observed-frame $24 \mu\text{m}$ flux and/or obscures the observed-frame $8 \mu\text{m}$ flux, or to the $7.7 \mu\text{m}$ PAH feature passing into the MIPS $24 \mu\text{m}$ band. We explore these possibilities further in Section 4.3.

⁷ For consistency with the IRAC power-law selection in Alonso-Herrero et al. (2006) and Donley et al. (2007), we assume an IRAC flux calibration uncertainty of 10%.

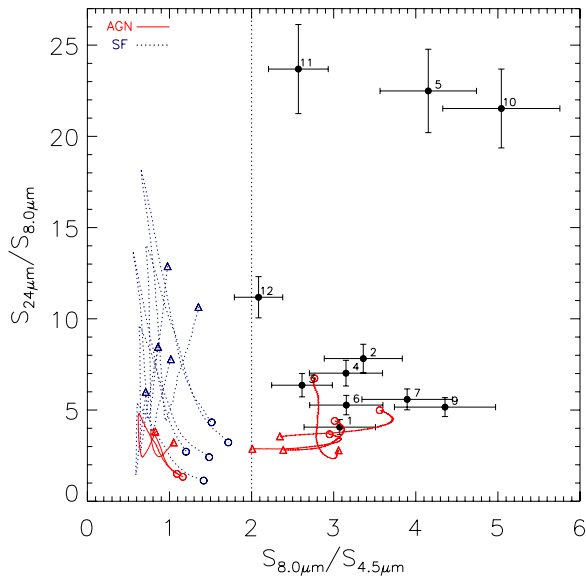


Figure 2. MIR colors of the IRBGs, where the numbers give the source ID. Overplotted are the redshifted ($z = 1-3$) templates of AGN from Polletta et al. (2008, TQSO, Seyfert 2, Seyfert 1.8, Mrk231) and Assef et al. (2008, AGN and AGN2) and of purely star-forming ULIRGS from Rieke et al. (2009). The two AGN templates with colors blueward of $S_{8.0}/S_{4.5} = 2$ are the Seyfert 1.8 and Seyfert 2 templates of Polletta et al. (2008). Triangles give the template colors at $z = 1$ and circles given the colors at $z = 3$. All of the IRBGs have $S_{8.0}/S_{4.5} > 2$ as expected only for AGN-dominated objects (e.g., Pope et al. 2008a). IRBG13, with its rapidly rising IRAC continuum, falls off the plot at values of $S_{8.0}/S_{4.5} = 12.8$ and $S_{24}/S_{8.0} = 8.1$.

(A color version of this figure is available in the online journal.)

4. IR SPECTRA

The IRS spectra of our 13 IRBGs are shown in Figure 3. To measure redshifts and determine the source of the emission (e.g., AGN or star formation), we simultaneously fit a power-law continuum and a star-forming template to each spectrum. For the star-forming templates, we adopt the starburst, luminous infrared galaxy (LIRG), and ULIRG templates of Rieke et al. (2009). While we allow the power-law component to be reddened according to the extinction law of Draine (2003), in no case do we require additional reddening to be applied to the star-forming templates.

Using a chi-squared minimization routine, we then fit the spectrum while leaving the template normalizations, power-law index, power-law extinction, and redshift as free parameters. To protect against local minima, we varied the assigned starting values for the parameters, and chose the input values that produced the fit with the lowest reduced chi-squared (if more than one minimum was found). Finally, to place errors on the fit parameters, we created 1000 simulated spectra for each source (based on the measured spectra and their associated Gaussian errors) and re-ran our fitting program on each. The errors quoted below for the redshifts (Section 4.2) and AGN fractions (Section 4.3) are taken to be the standard deviations in the resulting distributions of fit values. This procedure produces reasonable spectral fits for all sources except IRBG7, discussed below, although for four objects the lack of spectral features prevented direct redshift constraints.

4.1. IRBG7

IRBG7 has two spectral features and/or artifacts that impact the fit. The first is a sharp emission feature at $\lambda_{\text{obs}} \sim 21 \mu\text{m}$ or

$\lambda_{\text{emit}} \sim 7.6 \mu\text{m}$ assuming our best-fit redshift of $z = 1.76$ (for comparison, Murphy et al. 2009 measure a redshift of $z = 1.75$). This feature, which can be seen in the raw spectral data, could be strong $7.65 \mu\text{m}$ [Ne VI] emission that is partially blended with the $7.7 \mu\text{m}$ PAH emission.

The second strange feature in this spectrum is the apparently blue continuum at $\lambda \lesssim 18 \mu\text{m}$, present in both our reduction of the IRS data as well as that of Pope et al. (2008b, A. Pope 2009, private communication) and Murphy et al. (2009). If the AGN continuum fit is free to vary over all spectral indices, it settles on a blue slope of $\alpha = 1.69$ (where $f_\nu \propto \nu^\alpha$), despite its extremely red ($\alpha = -2.21$) IRAC power-law continuum. Such behavior, however, appears to be unphysical, for while the IRS slope need not match the IRAC slope, the two are generally close. In fact, the offset between the IRAC spectral slope (α_{IRAC}) and the IRS spectral slope (α_{IRS}) for the seven additional power-law galaxies in our sample ranges from 2% to 42%, with a mean (median) value of only 18% (16%).

We therefore adopt a revised method to fit the spectrum of IRBG7. First, we place an upper limit on the IRS AGN continuum slope by adjusting the measured IRAC slope of $\alpha = -2.21$ upward (blueward) by 18%, the mean offset between the IRAC power law and IRS slopes. With this assumed AGN continuum of $\alpha = -1.81$, we then perform an AGN-only fit at $\lambda > 18 \mu\text{m}$ to determine the AGN extinction that best fits the profile of the $9.7 \mu\text{m}$ silicate absorption feature. We then set the normalization of the AGN continuum by extrapolating the IRAC continuum fit from $8 \mu\text{m}$ to $14 \mu\text{m}$. When we do the same for the other power-law galaxies in the sample, we find that the mean offset between the predicted and observed $14 \mu\text{m}$ flux density is 35%. To place a lower limit on the AGN contribution, we therefore scale the AGN contribution downward until the $14 \mu\text{m}$ AGN flux density is 35% lower than predicted by the IRAC extrapolation, while allowing the star-forming contribution to vary so as to give the lowest reduced chi-squared. The resulting fit underpredicts both the short-wavelength emission and the $21 \mu\text{m}$ emission peak, as expected, but now places a robust lower-limit on the AGN's contribution to the MIR emission.

4.2. Redshifts

Of the 13 sources in our sample, 4 have optical/NIR spectroscopic redshifts from the literature (Szokoly et al. 2004; Swinbank et al. 2004; Davis et al. 2007). Using the IRS spectra, we determine reliable redshifts for an additional six sources, for an overall redshift completeness of $\sim 80\%$. The IRS redshifts derived for three of the four sources with prior optical/NIR redshifts agree to within $\Delta z \leq 0.1$ in all cases (The fourth source, IRBG4, has a power-law IRS spectrum from which no redshift estimate can be made).

Of the three remaining sources, two (IRBG1 and IRBG9) have power-law spectra and SEDs, and one (IRBG8) has both a spectrum dominated by power-law emission as well as questionable IRAC photometry due to its position near the edge of the IRAC field, thus preventing accurate spectroscopic or photometric redshift determination.

The mean and median redshifts of our sample, $z = 1.89$ and $z = 2.00$, respectively, agree quite well with the typical redshifts of similar samples. For instance, both Weedman et al. (2006a) and Houck et al. (2005) find median redshifts of $z = 2.1$, Yan et al. (2005) finds a median redshift of $z = 2.3$, and Polletta et al. (2008) finds a median redshift of $z = 2.2$.

Finally, with the exception of IRBG12, all of the sources lie at $z > 1.60$. The redshift of IRBG12, $z = 1.04$, is therefore

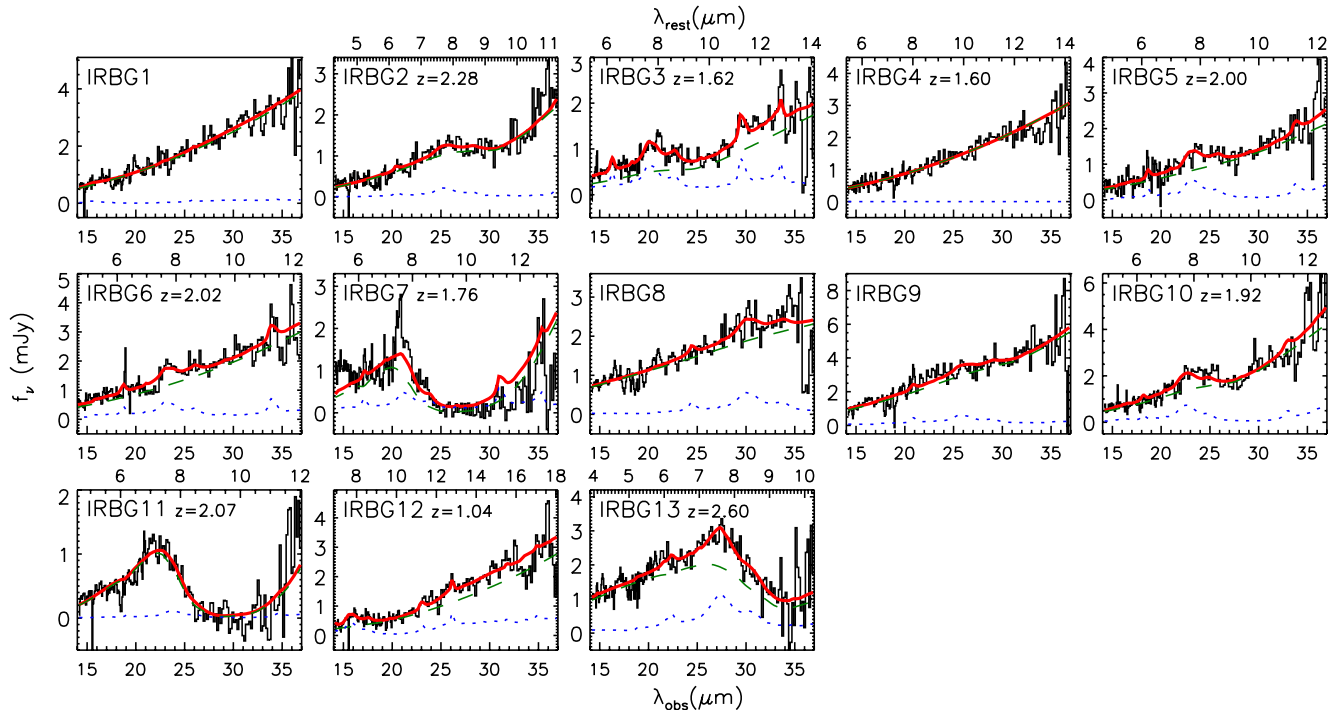


Figure 3. IRS spectra of the IRBGs. The green dashed line shows the observed contribution from the AGN whereas the blue dotted line shows the observed contribution from star formation. The overall fit is given by the red solid line.

(A color version of this figure is available in the online journal.)

quite low in comparison both to our and other (e.g., Houck et al. 2005; Yan et al. 2005; Weedman et al. 2006a; Polletta et al. 2008) samples of luminous IRBGs. This source’s low redshift, however, appears robust. The reduced chi-squared fit has 3 minima, one at $z = 0.11$, one at $z = 1.04$, and one at $z = 3.19$. As shown in Figure 1, however, this source has a weak $1.6 \mu\text{m}$ stellar bump that is well fit at optical-NIR rest-frame wavelengths by the $z \sim 1$ template of the starburst galaxy NGC 6090 from Polletta et al. (2006). We can therefore rule out the low and high redshift solutions from the IRS spectroscopy on the basis of the broadband SED.

4.3. Source of Power: AGN Activity or Star-formation?

The fraction of the overall IRS (14–37 μm) dust-obscured flux density arising from the AGN power-law component (e.g., the AGN fraction), the best-fit power-law indices, and the optical depths at 9.7 μm (for the power-law component) are shown in Table 2. On the basis of their MIR (14–37 μm) emission, all of the IRBGs in our sample are AGN dominated, with AGN fractions ranging from 71% to 100%. Six of the IRBGs are nearly pure power laws with AGN fractions exceeding 90%, three have hints of PAH emission with AGN fractions between 80% and 90%, and the remaining four have noticeable contributions from PAH features with AGN fractions <80%. For comparison, only 2 of the 13 SMGs from Pope et al. (2008b) and Murphy et al. (2009) have similarly derived AGN fractions exceeding 60%. One of these two sources is IRBG5 from our sample, and the other is an IRBG with a 24 μm flux density that fell below our flux cut of 700 μJy ($f_{24} = 303 \mu\text{Jy}$).

As discussed above, the mean offset between the IRAC and IRS spectral slopes of the power-law galaxies is only 18%. Furthermore, none of the power-law AGNs have IRAC and IRS slopes that differ by more than $\sim 40\%$, indicating that the power-law emission seen at rest-frame wavelengths of $\sim 1\text{--}3 \mu\text{m}$

continues up to $\sim 12 \mu\text{m}$, and possibly beyond, assuming a typical redshift of $z \sim 2$.

Recall, however, that three of the IRBGs in our sample (IRBG5, IRBG10, and IRBG11), have far-higher ratios of 24 μm to 8 μm flux than the rest ($S_{24}/S_{8.0} \gtrsim 20$, see Figure 2), due either to extremely high levels of extinction extending into the NIR (at $z = 2$, the 2.7 μm rest-frame emission is redshifted into the observed 8 μm band) or to a contribution from the 7.7 μm PAH feature. The IRS spectra suggest that both of the above scenarios contribute to the enhanced 24 μm flux densities of IRBG5 and IRBG10. At redshifts of $z = 2.00$ and $z = 1.92$, the 7.7 μm PAH feature, clearly visible in each of the spectra, serves to enhance the observed MIPS flux. However, star formation is responsible for only $\sim 25\%$ of the 24 μm flux density in these two sources. Removal of the star-forming flux therefore lowers the observed 24 μm to 8 μm flux ratios, but only to values of 15.9 and 17.6, still well above the ratios seen for the remaining sources. The power-law continuum at an observed wavelength of 8 μm is therefore likely to be suppressed, although shorter-wavelength spectral data would be needed to verify this hypothesis.

The remaining source, IRBG11, differs from the others in that the AGN accounts for 92% of the MIR flux density, and no noticeable contribution from PAH emission is seen in the spectrum. In this case, the large 24 μm to 8 μm flux ratio most likely results from extreme MIR obscuration. Indeed, this source shows one of the largest 9.7 μm opacities in our sample, $\tau_{9.7} = 5.0$, corresponding to an A_V of 92.5 if we assume the conversion of Draine (2003).

5. X-RAY PROPERTIES

As discussed in the introduction, the study of luminous IRBGs has suffered thus far from a relative lack of sensitive X-ray coverage in the fields where these sources have traditionally

Table 4
X-ray Properties

ID	T_X (s)	$f_{(0.5-2 \text{ keV})}$ ($\text{erg s}^{-1} \text{ cm}^{-2}$)	$f_{(2-8 \text{ keV})}$ ($\text{erg s}^{-1} \text{ cm}^{-2}$)	$f_{(0.5-8 \text{ keV})}$ ($\text{erg s}^{-1} \text{ cm}^{-2}$)	$\log L_{2-10 \text{ keV}}^a$ (erg s^{-1})	$\log N_H^b$ (cm^{-2})	$\log L_{2-10 \text{ keV, cor}}^c$ (erg s^{-1})
IRBG1	4.30E+05	8.52E-16	5.05E-15	6.29E-15	43.6	23.4 $^{+0.3}_{-0.3}$	44.3
IRBG2	1.57E+06	2.86E-15	7.50E-15	1.06E-14	44.2	23.0 $^{+0.1}_{-0.1}$	44.6
IRBG3	2.23E+05	<7.07E-17	1.37E-15 ^d	6.53E-16 ^d	<42.3	>23.6	>43.6
IRBG4	1.67E+06	5.58E-15	7.42E-15	1.30E-14	44.2	22.0 $^{+0.1}_{-0.1}$	44.2
IRBG5	1.65E+06	<4.00E-17	<3.26E-16	<2.06E-16	<42.3
IRBG6	1.92E+06	2.07E-16	2.48E-15	2.52E-15	43.0	23.6 $^{+0.0}_{-0.1}$	44.0
IRBG7	1.41E+06	1.52E-16	1.32E-15	1.40E-15	42.7	23.4 $^{+0.1}_{-0.2}$	43.6
IRBG8	7.16E+07 ^e	4.28E-15	1.04E-14	1.47E-14	44.3	22.8 $^{+0.3}_{-0.3}$	44.6
IRBG9	4.86E+07 ^e	<1.86E-16	<1.10E-15	5.39E-16 ^d	<42.9
IRBG10	5.10E+07 ^e	1.86E-16	<4.85E-16	5.11E-16	42.9	<22.8	<43.2
IRBG11	5.78E+07 ^e	<6.64E-17	<8.63E-17	<1.53E-16	<42.5
IRBG12	7.34E+07 ^e	<1.74E-16	<7.76E-16	<6.49E-16	<42.3
IRBG13	7.47E+07 ^e	<1.24E-16	<7.95E-16	<4.93E-16	<43.0

Notes.

^a Log of the rest-frame, non absorption-corrected 2–10 keV luminosity, calculated using the observed 0.5–2 keV flux, $\Gamma = 2.0$, and an assumed redshift of $z = 2.0$ for those sources lacking redshift constraints.

^b Estimated using the observed flux ratio and an intrinsic photon index of $\Gamma = 2$.

^c Log of the rest-frame, absorption-corrected 2–10 keV luminosity.

^d Low-significance X-ray detections: $\sigma(\text{IRBG3}, 0.5-8 \text{ keV}) = 4.8$; $\sigma(\text{IRBG3}, 2-8 \text{ keV}) = 5.5$; $\sigma(\text{IRBG9}, 0.5-8 \text{ keV}) = 2.1$.

^e Units of s cm^2 , nominal exposure time is 200 ks.

been identified (e.g., the *Spitzer* First-Look Survey, the NOAO Deep Wide Field Survey, and the SWIRE survey). As such, the X-ray analysis of IRBGs has lagged behind their study in the infrared, and to date, no studies have obtained both IRS spectra and deep X-ray imaging of a statistically significant sample of IRBGs selected independently of their X-ray properties. The deep X-ray coverage and complete IRS sampling of our uniformly selected IRBGs will therefore help to bridge the gap between prior X-ray and MIR spectral studies of these sources.

5.1. X-ray Detection Fraction

The X-ray data for the CDF-N, CDF-S, E-CDFS-S, and EGS come from Alexander et al. (2003), Luo et al. (2008), Lehmer et al. (2005), and Laird et al. (2009), respectively. At the position of the 13 IRBGs, the X-ray exposures range from ~ 200 ks to ~ 2 Ms, with a mean value of ~ 800 ks. Only 7 of the 13 IRBGs ($\sim 50\%$), however, are formally detected in the X-ray (e.g., are detected to high enough significance to be included in published X-ray catalogs). Their X-ray fluxes in the full (0.5–8 keV), hard (2–8 keV), and soft (0.5–2 keV) X-ray bands are given in Table 4. For sources in the EGS, we scale the published 0.5–10 keV and 2–10 keV fluxes to the bands defined above assuming an observed photon index of $\Gamma = 1.4$ (the observed photon index of the typical obscured AGN, and thus of the X-ray background, in this energy range, e.g., Marshall et al. 1980; Gendreau et al. 1995; Hickox & Markevitch 2006).

For the six sources not detected in the catalogs listed above, we searched for faint X-ray counterparts using the procedure outlined in Donley et al. (2005). Briefly, we first calculated the appropriate 60%, 70%, and 80% encircled energy radii (EER) for each source by exposure-weighting the EER, as measured using the lookup tables of Laird et al. (2009), for each individual *Chandra* observation. After measuring the source counts in each of the three apertures, we measured sky counts in 10,000 randomly placed apertures of the same size that (1) did not intersect the source aperture, that (2) lie within $1'$ of the source position, and that (3) did not contain a known X-ray source. In addition, we corrected the counts in each sky aperture to reflect

the exposure time measured for the source, and only allowed sky apertures in which the exposure differs from the source exposure by no more than 15%. We then fit a Poisson distribution to the resulting distribution of sky counts to determine the significance of any source detection, and chose the EER that maximized the source signal.

Of the six formally X-ray non-detected sources, IRBG3 is detected in both the full and hard bands to 4.8 and 5.5 σ above the sky, respectively, and IRBG9 is marginally detected in the full band, but only to 2.1 σ above the sky. The remaining four sources remain undetected in all bands, although one (IRBG5) lies too close to a known X-ray source to test for very faint X-ray emission. We place conservative 3σ upper limits on the flux of each X-ray-undetected source by adding any positive source counts to a 3σ upper limit on the measured sky background in the 70% EER, assuming the typical observed X-ray photon index of an obscured AGN, $\Gamma = 1.4$.

5.2. X-ray Obscuration

For the eight IRBGs with a formal or weak detection in the hard and/or soft X-ray bands, we crudely estimate the intrinsic column density using the hard to soft X-ray flux ratios, the measured redshifts (or $z = 2$ for sources lacking a secure redshift measurement), and an assumed intrinsic (e.g., unabsorbed) X-ray photon index of $\Gamma = 2.0$ (e.g., George et al. 2000). This method, commonly used to estimate the column densities of faint X-ray sources lacking sufficient counts for spectral fitting, is necessarily approximate in nature as it assumes an X-ray spectrum represented by a single absorbed power law and neglects the potential effects of more complicated spectral components such as the soft X-ray excess and/or Compton reflection. Nonetheless, column densities estimated in this way are broadly consistent with those determined via X-ray spectral fitting (see, for example, Appendix B of Perola et al. 2004). For instance, the column density we estimate for IRBG6, $\log N_H(\text{cm}^{-2}) = 23.6$, is in good agreement with the spectrally derived value of Alexander et al. (2005), $\log N_H(\text{cm}^{-2}) = 23.8$.

The column density estimates are given in Table 4. To place measurement errors on the columns, we take into account both the errors in the hard and soft X-ray flux, as well as the uncertainty on the redshift. For those sources lacking a secure redshift measurement, the redshift error is taken to be the standard deviation in the redshift distribution for the full sample of IRBGs, $\sigma_z = 0.42$. Of the eight sources for which X-ray-based estimates could be made, seven are formally obscured with $\log N_{\text{H}} (\text{cm}^{-2}) \geq 22$ and one has an upper limit consistent with significant obscuration ($\log N_{\text{H}} (\text{cm}^{-2}) \lesssim 22.8$).

From their infrared properties, we know that *all* of our sample contain strong AGNs. To place crude column density estimates on the X-ray-non-detected IRBGs, and to obtain independent estimates for the X-ray-detected sources, we follow Alexander et al. (2008b) and Lanzuisi et al. (2009) and explore the observed relationship between an AGN's rest-frame X-ray and MIR luminosity (e.g., Lutz et al. 2004)⁸. The position of our IRBGs in MIR/X-ray color space is shown in Figure 4, where the rest-frame $6 \mu\text{m}$ luminosities (νL_{ν}) have been estimated using the best-fit AGN contribution to the IRS spectra (which directly sample the rest-frame $6 \mu\text{m}$ emission at $z > 1.4$) and the rest-frame 2–10 keV luminosities have been estimated using the observed soft band flux (0.5–2 keV at $z = 0$, 1.5–6 keV at $z = 2$) and an assumed observed photon index of $\Gamma = 1.4$, typical of obscured AGN. The shaded region in Figure 4 gives the intrinsic luminosity-dependent relation of Maiolino et al. (2007), who drew their AGN sample from both low ($z < 0.2$) and high ($z = 2-3$) redshifts.⁹ As shown, the average *absorption-corrected* (e.g., intrinsic) luminosity ratio of the six sources in our sample with crude X-ray-derived column density estimates is consistent with the Maiolino et al. (2007) relation. The effect of various obscuring columns on the observed relation of Maiolino et al. (2007) is shown by dashed lines, where we again assume an intrinsic photon index of $\Gamma = 2.0$. We also assume for simplicity that the $6 \mu\text{m}$ emission from the torus is isotropic, i.e., that it does not depend on the obscuring column or on the angle at which the AGN/torus is viewed. If the torus is optically thick at MIR wavelengths (e.g., Pier & Krolik 1992; Heckman 1995; Buchanan et al. 2006), however, an obscured AGN would fall to both lower X-ray and lower MIR fluxes, thus increasing somewhat the column density estimated via this method.

For comparison, we also show the absorption-corrected colors of the Type 2 QSOs from Sturm et al. (2006), all of which fall in or above the Lutz et al. (2004) region, and the observed colors of the $z \sim 2$ Compton-thick AGNs from Alexander et al. (2008b), all of which fall below the $N_{\text{H}} = 10^{24} \text{ cm}^{-2}$ relation.¹⁰ Furthermore, we also plot the observed colors of the

⁸ We note that this analysis is only possible because our sources are AGN-dominated in the MIR. Furthermore, we are able to isolate the already-dominant AGN emission using the spectral decomposition described in Section 4. In general, however, for a source where the infrared emission is dominated by a strong star-forming component, the X-ray emission would appear anomalously faint in comparison and the column density would be greatly overestimated (see Georgakakis et al. 2010 for further discussion).

⁹ We assume the average IRS spectral slope of our sample, $\alpha = -1.94$, to convert the Maiolino et al. (2007) relation, initially defined at $6.7 \mu\text{m}$, to $6.0 \mu\text{m}$.

¹⁰ The source SMM J123600 + 621047 from Alexander et al. (2008b) corresponds to source IRBG5 in this work. Because of the slightly different procedures used to estimate the rest-frame X-ray and IR luminosities, however, our calculated values of $\log L_{2-10 \text{ keV}} (\text{erg s}^{-1}) = 45.4$ and $\log \nu L_{\nu} (\text{erg s}^{-1}) < 42.3$ differ slightly from those in Alexander et al. (2008b): $\log L_{2-10 \text{ keV}} (\text{erg s}^{-1}) = 45.3$ and $\log \nu L_{\nu} (\text{erg s}^{-1}) < 42.4$. For consistency, we plot the Alexander et al. (2008b) source using the values measured here.

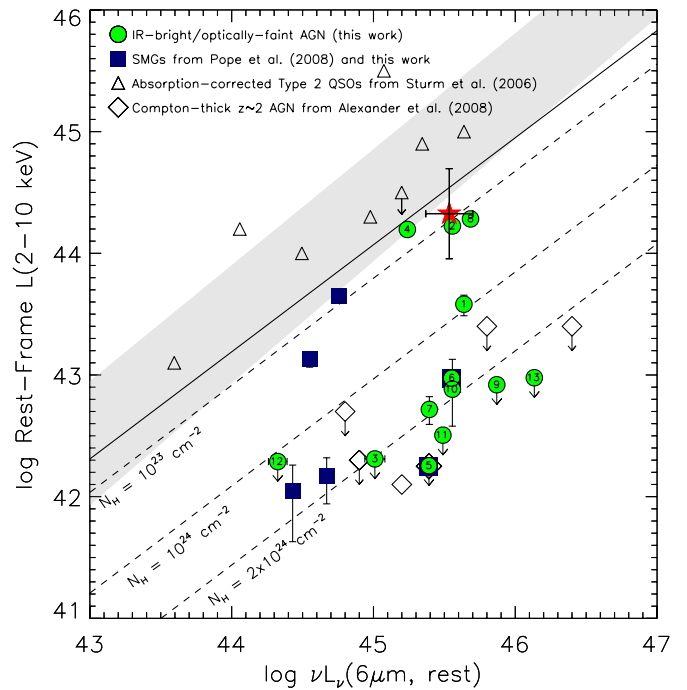


Figure 4. Rest-frame obscured X-ray luminosity vs. rest-frame $6 \mu\text{m}$ monochromatic luminosity, the values of which are given in Tables 2 and 4. The IRBGs are shown as circles. The intrinsic relation for local AGN (Lutz et al. 2004) and the intrinsic, luminosity-dependent relation of Maiolino et al. (2007, see footnote 9), which is based on both low and high redshift ($z \sim 2$) AGNs, are given by the shaded region and solid line, respectively. As indicated by the red star, the *absorption-corrected* (e.g., intrinsic) luminosity ratio of the six sources in our sample with crude X-ray-derived column density estimates is broadly consistent with the Maiolino et al. (2007) and Lutz et al. (2004) relations (the error bars represent the standard deviation in the distribution of X-ray and $6 \mu\text{m}$ luminosities). Dashed lines give the expected observed relations for AGNs obscured by column densities of $N_{\text{H}} = 10^{23}$, 10^{24} , and $2 \times 10^{24} \text{ cm}^{-2}$, calculated assuming an intrinsic X-ray photon index of $\Gamma = 2$. For comparison, the observed X-ray and intrinsic $6 \mu\text{m}$ luminosities of the Compton-thick AGN from Alexander et al. (2008b) are shown as diamonds and a sample of SMGs containing AGN drawn both from this work and from Pope et al. (2008b) are shown as squares. The absorption-corrected values for the Type II AGN from Sturm et al. (2006) are shown as triangles. Based on this luminosity ratio, 5/13 IRBGs are strong Compton-thick candidates with predicted columns of $N_{\text{H}} \geq 2 \times 10^{24} \text{ cm}^{-2}$, and 5 additional sources lie near the Compton-thick/heavily obscured boundary ($N_{\text{H}} \gtrsim 10^{24} \text{ cm}^{-2}$).

(A color version of this figure is available in the online journal.)

six SMGs with a well-measured MIR AGN contribution from either Pope et al. (2008b, C1, C3, GN04, GN06, GN07) or this work (both IRBG5, which corresponds to source C1 in Pope et al. (2008b), and IRBG6 are SMGs). For the Pope et al. (2008b) sources, we estimate the intrinsic $6 \mu\text{m}$ luminosity using their Figure 3 for which they performed spectral fitting similar to that described in Section 4. X-ray flux measurements were taken from Alexander et al. (2003) when available (C1 and GN04), and were calculated as described in Section 5.1 otherwise. Of the six SMGs, three (IRBG6, C3, GN04) are detected in the X-ray to high significance, two (GN06 and GN07) are weakly detected at 6.2σ and 3.3σ above the background, respectively, and one (C1/IRBG5) remains X-ray undetected.

As shown in Figure 4, three of our 13 sources (IRBG2, IRBG4, and IRBG8) appear to be obscured yet Compton thin ($N_{\text{H}} \sim 10^{23} \text{ cm}^{-2}$); the remaining 10 lie near or above the Compton-thick boundary ($N_{\text{H}} \gtrsim 10^{24} \text{ cm}^{-2}$). This high fraction of Compton-thick candidates ($\sim 80\%$) is significantly larger than that found by Lanzuisi et al. (2009, 18%) thanks to the far deeper

X-ray data ($T_X = 200$ ks to 2 Ms compared to $T_X = 5\text{--}70$ ks). Furthermore, there is at least rough agreement between the column densities estimated above and those estimated here. For instance, of the three sources with X-ray/MIR luminosity ratios indicative of column densities of $\log N_H$ (cm^{-2}) $\lesssim 23$, all have X-ray-derived column densities of $22 \leq \log N_H$ (cm^{-2}) ≤ 23 . Of the remaining three sources with X-ray-derived column densities (IRBG1, IRBG6, and IRBG7), two are identified as Compton-thick candidates in Figure 4 and one (IRBG1) has an estimated column that falls just short of $\log N_H$ (cm^{-2}) = 24. While their X-ray-derived columns ($\log N_H$ (cm^{-2}) = 23.4–23.6) place them just outside the Compton-thick regime, column densities based on low S/N flux ratios are often unable to distinguish Compton-thick AGNs from their most heavily obscured, yet Compton-thin, counterparts (see, for example, Figure 3 of Alexander et al. 2008b). On the basis of the X-ray and X-ray/MIR-derived column densities, we therefore conclude that all of the sources in our sample are likely to be X-ray obscured ($\log N_H$ (cm^{-2}) ≥ 22), and as many as 10 ($\sim 80\%$) may be Compton thick. Furthermore, at least five of these sources ($\sim 40\%$) lie at predicted column densities of $> 2 \times 10^{24}$ cm^{-2} , and are therefore strong Compton-thick candidates.

One of these strong Compton-thick candidates, IRBG5, was previously identified as a potential Compton-thick quasar by both Alexander et al. (2008b) and Georgantopoulos et al. (2009) and is also one of the SMGs plotted in Figure 4. Its heavily obscured nature, however, is not unique among the sample of SMGs with measurable AGN contributions in the MIR. In fact, four of the six SMGs plotted in Figure 4 ($\sim 70\%$) are Compton-thick candidates. Our results are therefore in agreement with those of Alexander et al. (2005), who found that 80% of SMGs containing X-ray-detected AGNs are likely to be heavily obscured ($\log N_H$ (cm^{-2}) $\gtrsim 23$) and potentially Compton thick. This similarity between the column density distributions of the IRBG and SMG samples underscores the potential relationship between these two classes of objects, discussed in more detail in Sections 7 and 8.

5.3. X-ray Luminosity

The observed and absorption-corrected X-ray luminosities of the IRBGs are given in Table 4. The mean, non-absorption-corrected 2–10 keV rest-frame luminosity of the 7 sources with soft-band detections (calculated as described in Section 5.2) is $\log L_{2-10}(\text{erg s}^{-1}) = 43.9$, which rises to $\log L_{2-10}(\text{erg s}^{-1}) = 44.3$ when we apply the absorption corrections to the 6 sources with X-ray-derived N_H measurements.

As discussed in Section 5.2, an AGN’s intrinsic X-ray luminosity can also be estimated from its rest-frame 6 μm luminosity (see Figure 4). This technique has the added advantage that it can be applied to all of the sources in the sample, regardless of whether they are formally detected in the X-ray. Assuming a redshift of $z = 2$ for the 3 sources lacking redshift estimates, we find a mean intrinsic 2–10 keV luminosity of $\log L_{2-10}(\text{erg s}^{-1}) = 44.6 \pm 0.4$ for the 13 sources in our sample. This value is only slightly higher than the estimate made above for the sources with X-ray-derived column density estimates ($\log L_{2-10}(\text{erg s}^{-1}) = 44.3$), as would be expected if the flux ratio method underestimates the column densities of the most heavily obscured sources. Furthermore, Figure 4 suggests that essentially all of the sources in our sample (with the exception of IRBG12, whose redshift is only $z = 1.04$) have intrinsic X-ray luminosities that lie above the canonical division between

low-luminosity Seyfert galaxies and high-luminosity QSOs, $\log L_x(\text{erg s}^{-1}) = 44$. The IRBGs in our sample are therefore Type 2 QSOs, at least from the X-ray perspective.

5.4. Correlation between X-ray and IR Properties

All three of the sources in our sample that are optically thick at 9.7 μm ($\tau_{9.7 \mu\text{m}} \sim 1\text{--}5$) are Compton-thick candidates with MIR/X-ray-estimated column densities of $N_H \gtrsim 2 \times 10^{24}$ cm^{-2} . The seven additional Compton-thick candidates, however, display little to no silicate absorption ($\tau_{9.7 \mu\text{m}} \leq 0.5$). While it is possible that the three sources lacking solid redshift estimates (one of which is a Compton-thick candidate) could have a silicate feature redshifted out of the observable band ($z \geq 2.6$), the highest confirmed redshift in our sample is that of IRBG13, $z = 2.6$, a source with a prominent absorption feature. Given the average sample redshift of $z = 2$ and the low frequency of silicate absorption among the sources in our sample with confirmed redshifts, it therefore seems unlikely that the three sources lacking redshift information (and observable silicate features) lie at $z > 2.6$ and have significant silicate absorption.

It therefore appears clear that while silicate absorption is more likely among heavily X-ray-obscured IRBGs, strong silicate absorption need not accompany X-ray obscuration. Similar conclusions were drawn by Brand et al. (2008) for a sample of luminous ($f_{24} > 2$ mJy) IRBGs in the NOAO Deep Wide-Field Survey, Sajina et al. (2008) for a sample of $z \sim 1\text{--}3$ *Spitzer*-selected ULIRGS, and Sturm et al. (2005), who show that bright ($F_{15 \mu\text{m}} > 0.3$ mJy) X-ray-selected Type 2 AGNs can show unabsorbed power-law continua in the IR despite heavy obscuration in the X-ray. This apparent discrepancy between X-ray and MIR measures of obscuration could be due to an additional component of absorbing material that blocks the X-ray, but not the IR, emission region (e.g., Shi et al. 2006). Alternatively, it could result from the filling-in of the silicate feature by an additional component of extended hot dust that lies beyond the obscuring torus, arising, for example, from the ionization cones as in NGC 1068, the prototypical Compton-thick AGN in the local universe (Mason et al. 2006; Efstathiou et al. 1995).

6. STAR FORMATION RATES

For the seven IRBGs with detectable PAH emission (i.e., AGN fractions $< 90\%$), we place limits on the SFRs using (1) the star-forming contribution to the observed-frame 24 μm emission (in lieu of direct estimates based on the weakly detected PAH emission features) and (2) the observed radio emission.

6.1. 24 μm Emission

To measure the 24 μm flux density arising from star formation alone, we convolve the star formation component of our IRS fit with the MIPS 24 μm passband. We find that in the sources with detectable PAH emission, $\sim 25\%$ of the total 24 μm flux density can be attributed to star formation. We then use the redshift-dependent scaling relation of Rieke et al. (2009) to convert the observed MIR flux to a SFR, assuming the median sample redshift of $z = 2$ for those sources lacking secure redshift estimates (for further details, see Rieke et al. 2009). With the exceptions of IRBG13, whose anomalously high SFR estimate of $2 \times 10^4 M_\odot \text{yr}^{-1}$ will be discussed below, and IRBG12, whose estimated SFR is $\sim 150 M_\odot \text{yr}^{-1}$, the resulting SFRs range from ~ 1000 to $2000 M_\odot \text{yr}^{-1}$. No meaningful constraints can be

placed on the SFRs of those sources with AGN contributions in excess of 90% ($\text{SFR} \leq 7000\text{--}5 \times 10^4 M_{\odot} \text{ yr}^{-1}$).

These estimates, however, are based on a relationship derived from local starburst, LIRG, and ULIRG templates. At high-redshift, luminous star-forming galaxies exhibit strong PAH features typical of less-luminous local galaxies, due perhaps to extended star formation or lower metallicity (e.g., Sajina et al. 2007; Papovich et al. 2007; Pope et al. 2008b; Rigby et al. 2008; Farrah et al. 2008; Murphy et al. 2009; Menéndez-Delmestre et al. 2009). Local templates are therefore likely to overestimate the intrinsic $24 \mu\text{m}$ flux (and therefore the SFR) of high- z ULIRGS significantly at $L(\text{TIR}) = 10^{13} L_{\odot}$, the typical luminosities of luminous IRBGs (see Rieke et al. 2009; Tyler et al. 2009). Additional uncertainties in the derived SFRs arise from the lack of luminous $L(\text{TIR}) > 2 \times 10^{12} L_{\odot}$ ULIRGS in the local universe from which to calibrate the SFR relation. The IR-derived SFRs of the IRBGs should therefore be taken as rough upper limits on the true SFRs.

6.2. Radio Emission

To place an independent constraint on the SFRs, we therefore consider the 1.4 GHz radio flux density. Of the seven IRBGs with detectable PAH emission, six have radio counterparts in the catalogs of Richards (2000), Ivison et al. (2007), or Kellermann et al. (2008). Assuming a radio spectral index of $\alpha = -0.7$, where $f_{\nu} \propto \nu^{\alpha}$, we K -correct the observed radio flux and use the relation of Rieke et al. (2009) to estimate the SFR. With the exception of IRBG13, whose radio-derived SFR falls just short of the IR-derived SFR, the radio SFRs exceed the IR SFRs by factors of $\sim 1.2\text{--}10$, suggesting that a significant fraction of the radio flux density comes not from star formation, but from AGN activity. Therefore, the radio-derived SFRs again represent only an upper limit on the true star formation activity.

To isolate the star-forming contribution to the radio emission, we therefore turn to the radio-infrared correlation, characterized by the parameter $q_{24} = \log(f_{24 \mu\text{m}}/f_{1.4 \text{ GHz}})$. By using this correlation together with the measured star-forming contribution to the $24 \mu\text{m}$ flux density to calculate the star-forming radio flux density and then the SFR, we again utilize the MIR emission as a proxy for the SFR. This method, however, allows us to calibrate the SFR using the observed radio/SFR correlation in place of the $24 \mu\text{m}$ /SFR correlation discussed above.

A number of different studies have attempted to quantify q_{24} and have returned values ranging from 0.52 (Beswick et al. 2008) to 1.39 (Boyle et al. 2007). Here, we adopt the luminosity-dependent q_{24} relation of Rieke et al. (2009) which is based on the local IRAS bright galaxy sample (BGS) and for which $q_{24} = (-1.275 \pm 0.756) + (0.224 \pm 0.066) \times \log L(\text{TIR})/L_{\odot}$ at $\log L(\text{TIR})/L_{\odot} > 11$. At $\log L(\text{TIR})/L_{\odot} = 13.0$, the typical total infrared luminosity of luminous IRBGs (Tyler et al. 2009), $q_{24} = 1.64$.

The observed value of q_{24} also varies with redshift as the IR spectral features pass through the $24 \mu\text{m}$ band. To correct for this variation, we adopt the observed q_{24} redshift evolution of Ibar et al. (2008), who found that $q_{24} = (0.85 \pm 0.01) + (-0.20 \pm 0.01) \times z$. Not surprisingly, this observed redshift evolution is reproduced by the $\log L(\text{TIR})/L_{\odot} \sim 12.0$ templates of Rieke et al. (2009). After scaling the Ibar et al. (2008) relationship upward to match the Rieke et al. (2009) result at $z = 0$, we used the resulting correlation and our estimate of the star-forming $24 \mu\text{m}$ flux density to determine the expected radio emission from star formation.

We find that star formation accounts for 3%–23% of the total radio emission in our sources. Again with the exceptions of IRBG12 and IRBG13, whose estimated SFRs are $\sim 1600 M_{\odot} \text{ yr}^{-1}$ and $20 M_{\odot} \text{ yr}^{-1}$, respectively, we derive SFRs of $\sim 200\text{--}400 M_{\odot} \text{ yr}^{-1}$ using the star-formation-dominated radio emission. Because the high- z ULIRGS/HyperLIRGS in our sample are likely to have star-forming emission similar to that of local LIRGS/ULIRGS (see Section 6.1), however, the true intrinsic value of q_{24} is likely to be lower than the value assumed above. The estimated SFRs can be therefore be taken as lower limits, subject of course to the intrinsic scatter in the radio/IR correlation.

6.3. The High SFRs of Luminous IR-bright/Optically-faint Galaxies

To summarize, five of the seven IRBGs in our sample with detectable PAH emission and/or radio counterparts have estimated SFRs in the range of ~ 200 to $2000 M_{\odot} \text{ yr}^{-1}$. The SFR of IRBG12 ($\sim 20\text{--}150 M_{\odot} \text{ yr}^{-1}$) is lower than the others because of its significantly lower redshift ($z = 1.04$). The SFR of IRBG13, however, is anomalously high: $1.6\text{--}2.0 \times 10^4 M_{\odot} \text{ yr}^{-1}$. This overestimation likely stems from the fact that both an AGN+SF fit *and* an AGN-only fit reasonably reproduce the IRS spectrum ($\chi^2_{\nu} = 0.79$ and 0.85 , respectively). While potential AGN-only fits likewise exist for many of the sources in our sample, IRBG13 has the smallest offset in the reduced χ^2 values of the AGN+SF and AGN-only fits and is therefore the source for which the origin of the IR emission is most uncertain.

The SFRs derived above are clearly approximate in nature. Nevertheless, two of the seven sources examined above (IRBG5 and IRBG6) are known SMGs, heavily dust-enshrouded sources with typical SFRs of $500\text{--}2000 M_{\odot} \text{ yr}^{-1}$ (Swinbank et al. 2004; Alexander et al. 2005). As their IR properties are typical of the rest of our sample, it therefore seems likely that our estimated SFRs of $200\text{--}2000 M_{\odot} \text{ yr}^{-1}$ reasonably approximate the high level of star formation present in luminous IRBGs. Furthermore, our estimated SFRs are in agreement with the results of Tyler et al. (2009), who find via far-infrared measurements that approximately a third of IRBGs similar to those selected here have indications of star formation at a level that produces a substantial fraction of their bolometric luminosities, which are typically $10^{13} L_{\odot}$ (Tyler et al. 2009). Finally, such SFRs are also in agreement with the predictions of Narayanan et al. (2010b), who find that luminous IRBGs are best modeled by gas rich mergers undergoing rapid AGN growth and/or star formation at rates of $\sim 500\text{--}1000 M_{\odot} \text{ yr}^{-1}$.

Presumably, the objects with detected star formation represent the high end of a continuous luminosity function, where the lower levels of star formation are masked by the AGN outputs. That is, it is likely that these sources are in general characterized by star formation in the high-LIRG to ULIRG range, even though their MIR ($14\text{--}37 \mu\text{m}$) luminosities are AGN dominated.

7. HOST GALAXY MORPHOLOGIES

Because of the $\sim 30\%$ overlap of IRBG and SMG samples, as well as their similar redshift distributions, surface densities, and clustering properties, several authors have suggested that luminous IRBGs may evolve from SMGs (e.g., Dey et al. 2008; Pope et al. 2008a; Brodwin et al. 2008; Busmann et al. 2009; Narayanan et al. 2010a, 2010b). Furthermore, early studies of SMGs suggested that $61\% \pm 21\%$ may be in

the early stages of a major merger (Conselice et al. 2003b), although, on the basis of asymmetry measurements alone, more recent work has suggested that SMGs are no more likely to be undergoing major mergers than lower-luminosity high-redshift galaxies (Swinbank et al. 2010). While this work has called into question the uniqueness of the role that mergers play in these systems, the merger-driven origin of both SMGs and luminous IRBGs is supported by the GADGET2 simulations of Narayanan et al. (2010a, 2010b), who find that both samples naturally arise from gas-rich mergers, with SMGs representing the early, star formation dominated phase of the merger, and IRBGs representing the later phase of final coalescence in which star formation and obscured black hole growth both proceed at rapid rates (see Figure 1 in Hopkins et al. 2008). If this scenario is correct, luminous IRBGs should therefore exhibit signs of recent merger activity, although one might expect them to be more dynamically relaxed than their SMG predecessors.

7.1. Comparison between IRBGs and SMGs

Previous morphological studies of IRBGs have used targeted *HST* and Keck AO observations in the Bootes Field of the NOAO Deep Wide-Field Survey to (1) measure their typical sizes and shapes via Sersic fitting and GALFIT galaxy decomposition and to (2) characterize their morphologies on the basis of the Gini, M_{20} , and concentration indices (Bussmann et al. 2009; Melbourne et al. 2009). They conclude that IRBGs are preferentially found in disk-like galaxies, and only $\sim 15\%$ show multiple resolved components indicative of ongoing mergers, far lower than the $\sim 50\%$ interaction rate found for the average $z = 2$ ULIRG and the $\sim 60\%$ merger rate estimated for SMGs (Conselice et al. 2003b; Dasyra et al. 2008; Bussmann et al. 2009; Melbourne et al. 2009). However, IRBGs do appear to have smaller projected sizes ($r_{\text{Petrosian}} = 0'.5\text{--}1'.5$) than SMGs ($r_{\text{Petrosian}} = 0'.5\text{--}2'.5$), suggesting that they may in fact represent a later, more relaxed phase of a major merger (Bussmann et al. 2009).

To expand upon these studies and further test whether IRBGs are the product of major mergers, we directly compare below the morphologies of IRBGs and SMGs in a self-consistent manner. Because IRBG5 and IRBG6 are confirmed SMGs, we treat these two sources separately in the analysis below. We also note that because the EGS does not yet contain deep sub-mm coverage, it is possible that one or more of the EGS IRBGs could also be SMGs. Pope et al. (2008a), however, found an SMG fraction of only 30% among luminous IRBGs. As the fraction of SMGs in our sample of eight IRBGs with deep ACS coverage is already $\sim 25\%$, we therefore expect little to no additional contamination by SMGs in our morphological sample.

We select as a comparison sample of SMGs those sources in the GOODS-N field (Pope et al. 2005) with redshifts and apparent magnitudes consistent with those of the IRBGs: $1 < z < 3$ and $I < 26$, and confirm that none are also IRBGs (although GN25 has a high f_{24}/f_R of ~ 900 ; Cowie et al. 2004; Pope et al. 2006). The observed-frame *i*-band images of the eight IRBGs and eight SMGs with deep ACS imaging from GOODS or the EGS are shown in Figure 5.

7.1.1. Merger Fraction

To quantitatively compare the morphologies of these two samples, we calculate the Petrosian radii and concentration (C) and asymmetry (A) indices using the approach of Conselice et al. (2000) and the error-estimation method of Shi et al.

(2009), and confirm excellent agreement between our measured parameters and those of Shi et al. (2009) for the two sources that lie in both samples: IRBG5 and IRBG6 (Y. Shi 2009, private communication).

Of these parameters, the asymmetry index is the most relevant as it tends to be high ($A > 0.35$ in the local universe) when merging galaxies are undergoing either their first pass or their final coalescence (Conselice et al. 2003a; Lotz et al. 2008). We caution, however, that this index is designed to measure the asymmetry within the Petrosian radius ($r_{\text{Petrosian}}$) of the primary source. If the merging galaxies are separated by a large distance (as occurs, for example, during the merger stages between first pass and final coalescence), the secondary source will fall outside of the Petrosian radius of the primary source and the index will be low. Furthermore, surface brightness dimming causes the observed asymmetry to decrease with increasing redshift. While the correction for this effect is somewhat uncertain, Conselice et al. (2005) estimate an offset of $\Delta A = -0.15$ between $z = 0$ and $z = 2$ for irregular galaxies. As the Shi et al. (2009) error method results in measured asymmetries 0.05 lower than those found by the minimum error method of Conselice et al. (2000), we therefore adopt a merger index of $A \geq 0.15$ for our $z \sim 2$ sample.¹¹

The measured concentration and asymmetry indices are shown in Figure 6. By these measures alone, the IRBGs and SMGs appear to have similar morphologies. Furthermore, all of the sources with clear double nuclei have $A > 0.15$, as expected. Several SMGs, however, do indeed have nearby counterparts that lie outside the Petrosian radius of the primary source. If we therefore count as mergers all sources with either $A > 0.15$ or nearby counterparts that fall outside $r_{\text{Petrosian}}$ (e.g., GN22, GN20.2, GN20), we find that five of the seven ($\sim 70\%$) IRBGs and five of the eight ($\sim 60\%$) SMGs are merger candidates.

It is also worth noting that two of the three IRBGs which are optically thick at $9.7 \mu\text{m}$ (IRBG11 and IRBG13) are strong merger candidates with large asymmetries and clearly disturbed morphologies. The third, IRBG7, falls too near the edge of the ACS image to accurately calculate the asymmetry. Nonetheless, it appears to lie at the edge of a large patch of diffuse emission, potentially due to an ongoing merger (see Figure 5). As discussed in Section 5.4, these three optically thick sources are the only Compton-thick candidates with strong silicate absorption. It therefore appears plausible that ongoing mergers are at least partially responsible for the high degree of MIR obscuration in these heavily X-ray-obscured IRBGs. In their sample of local ULIRGs, Veilleux et al. (2009) similarly find that the depth of the $9.7 \mu\text{m}$ silicate feature is generally largest during the close pre-merger and merger stages. They caution, however, that this correlation suffers from a large degree of scatter, likely due to variations in both the initial conditions (e.g., the structure, surface mass density, and gas fractions of the infalling galaxies) and specific characteristics (e.g., orbital geometry and mass ratio) of the mergers themselves. This scatter may explain why the three remaining merger candidates (IRBG5, IRBG6, and IRBG10) show little to no MIR obscuration ($\tau_{9.7 \mu\text{m}} = 0.0\text{--}0.3$).

¹¹ We note that Shi et al. (2009) find a slope ($\Delta A/\Delta z$) between $z = 0$ and $z = 1$ that is twice that of Conselice et al. (2005) when using local LIRGs as input. It therefore remains possible that galaxies in our sample with $A < 0.15$ are undergoing mergers as well.

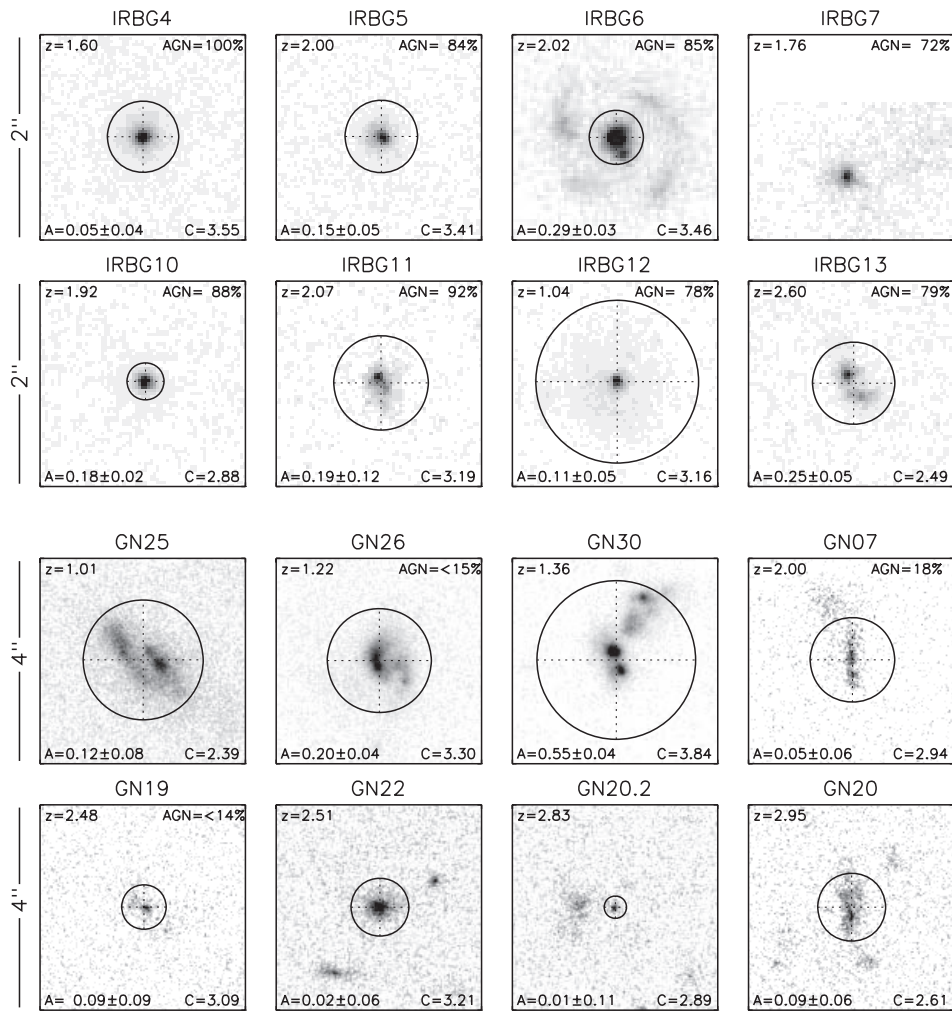


Figure 5. GOODS and AEGIS ACS *i*-band images of the 8 IRBGs with deep ACS coverage (top, image diameter of 2'') and the 8 GOODS-N SMGs from the literature with similar redshifts and *i*-band magnitudes (bottom, image diameter of 4''). The redshift and IRS-derived AGN fraction are given in the top left and right corners of the image, and the asymmetry and concentration indices for each galaxy are given in the bottom left and right corners of each image, respectively. The redshifts and AGN fractions for the SMGs come from Pope et al. (2006, 2008b) and Murphy et al. (2009). The circle gives the measured Petrosian radius, and the cross-hairs indicate the rotation center chosen by the asymmetry algorithm. Because it extends beyond the edge of the image, we are unable to estimate a reliable Petrosian radius or morphological indices for IRBG7.

7.1.2. Physical Size

While a majority of both SMGs and IRBGs appear to be sufficiently disturbed to be classified as major mergers, these two samples do appear to differ in their physical size, as inferred by Bussmann et al. (2009). A histogram of the Petrosian radii in physical units of kpc is shown in Figure 7. The mean $r_{\text{Petrosian}}$ of the SMGs, 6.8 ± 3.7 kpc, is nearly twice that of the IRBGs, 3.7 ± 1.8 kpc. If we exclude the three lowest-redshift SMGs with $z < 1.4$, the mean $r_{\text{Petrosian}}$ of the SMGs drops to 4.5 ± 2.0 kpc, suggesting that the apparent offset in physical size may be driven at least in part by evolution in the SMG population. Swinbank et al. (2010), however, detect no significant size evolution in either the optical or NIR radii of a sample of 25 SMGs. Furthermore, they find a mean optical (NIR) Petrosian radius of 6.9 ± 0.7 kpc (7.7 ± 0.6 kpc) for their SMG sample, consistent with our results and again a factor of ~ 2 higher than observed for the IRBGs.

This apparent offset in size may be a natural byproduct of the merger hypothesis, as the Petrosian radius of a merger remnant peaks strongly during both the first pass and the final merger stages and can easily obtain a value twice that of

the pre-merger, maximal separation (when only one galaxy is contained within the Petrosian radius), and post-merger stages (Lotz et al. 2008, J. Lotz 2009, private communication). An offset in $r_{\text{Petrosian}}$ of a factor of $\lesssim 2$ is therefore consistent with the hypothesis that SMGs are observed in the first stages of a major merger whereas IRBGs represent a post-merger phase following the final coalescence. What remains more difficult to explain, however, are the simultaneously *large* asymmetries and *small* radii of the IRBGs, as these two parameters should both peak at approximately the same stages during the merger. Larger samples of such sources are clearly needed to resolve this apparent discrepancy.

8. DISCUSSION

Several authors have suggested that IRBGs and SMGs may be evolutionarily related, each representing a different phase in the major-merger scenario originally proposed by Sanders et al. (1988) (e.g., Brodwin et al. 2008; Dey et al. 2008; Pope et al. 2008a; Coppin et al. 2010; Narayanan et al. 2010a, 2010b). To test this hypothesis, we explore below the agreement between the properties of the IRBG and SMG samples, as

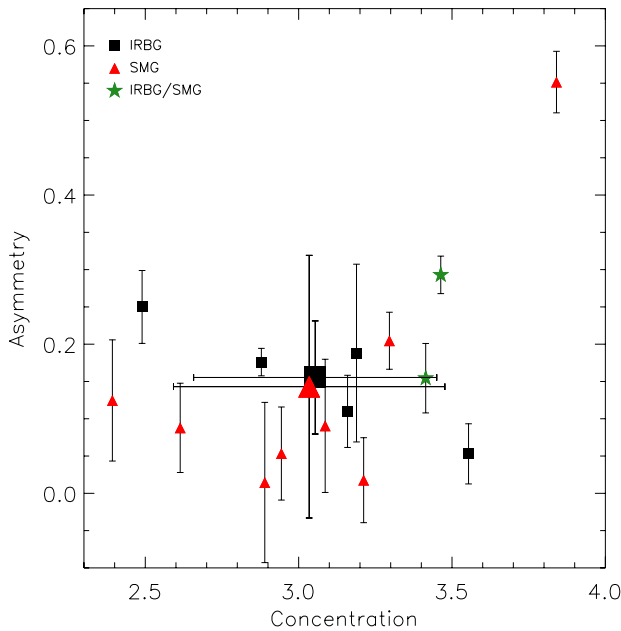


Figure 6. Asymmetry vs. concentration indices for the IRBGs (black squares), SMGs (red triangles), and sources that meet both criteria (green stars). The mean properties and standard deviations of the IRBG and SMG samples are shown by large symbols. As noted in Section 7.1.1, the measured asymmetry will be low when merging galaxies lie at large separations, as is the case for many of the SMGs. To calculate a merger fraction, we therefore consider both the measured asymmetry and the fraction of sources with nearby neighbors.

(A color version of this figure is available in the online journal.)

measured here and in the literature, and the major-merger model.

The major-merger (e.g., 3:1 or greater mass ratio) scenario, as presented by Hopkins et al. (2008), proceeds as follows. During the merging galaxies' first pass, star formation activity begins to increase with concurrent AGN activity occurring only under certain orbital geometries and/or when the host galaxies' disks are particularly unstable. As the galaxies undergo final coalescence, however, massive inflows power both strong starburst activity and heavily obscured, yet rapid, black hole growth. Eventually, feedback from the black hole and from supernovae disperse the remaining gas in a brief "blowout" phase characterized by a dust-obscured, yet Type 1, AGN. Finally, when the gas and dust have been fully dispersed, the source appears as an unobscured quasar (unless viewed through the canonical torus). The general picture is therefore one in which a major-merger fuels both star formation and black hole growth (thus leading to the observed M_{BH}/σ relation), with star formation dominating at early times, and AGN activity at later times.

Before continuing, it is worth noting that this model is almost certainly an oversimplification. As emphasized by Veilleux et al. (2009), the internal structure of the merging galaxies, the orbital parameters (e.g., prograde or retrograde), the mass ratio, and sub-resolution physics will ultimately determine the evolutionary path followed by any one merging galaxy pair, leading to variations on the model presented above and scatter in the observed correlations. Nonetheless, the general picture presented above should hold *on average* if this process is responsible for the SMG and IRBG phenomena.

In the context of this model, SMGs are assumed to represent the early, star-formation-dominated phase of the major merger, and IRBGs the later, AGN-dominated phase. To first order,

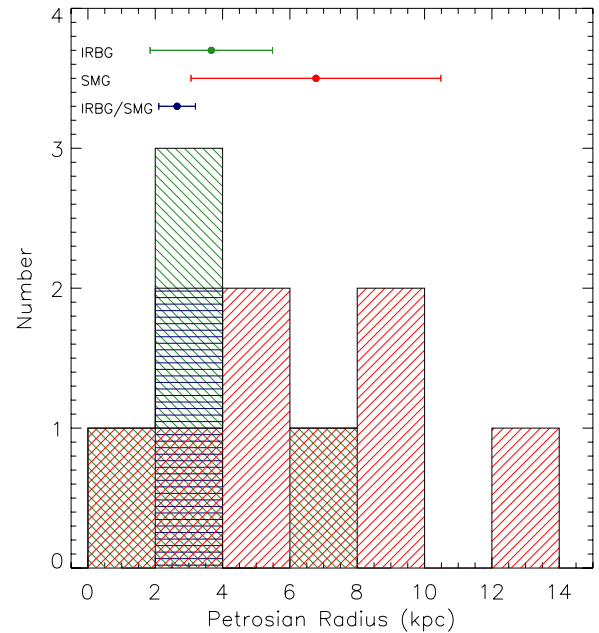


Figure 7. Petrosian radii of the IRBGs (green histogram, angle = -45°), SMGs (red histogram, angle = 45°), and sources that meet both criteria (blue histogram, angle = 0°). The mean radii (and standard deviations) for the three samples are shown at the top of the plot.

(A color version of this figure is available in the online journal.)

this progression is supported by the fact that while $\sim 85\%$ of SMGs are star-formation-dominated in the MIR (Pope et al. 2008b; Hainline et al. 2009; Coppin et al. 2010), and nearly all luminous IRBGs are AGN dominated in the MIR, there is an $\sim 30\%$ overlap in the SMG and IRBG populations, at least for samples extending down to $f_{24} \geq 100 \mu\text{Jy}$ (Pope et al. 2008a). Furthermore, the SMGs that also meet the IRBG criterion tend to have the largest AGN contributions, and are therefore likely candidates to be undergoing a transition from star formation to AGN dominance (e.g., Pope et al. 2008a; Coppin et al. 2010).

In addition, while SMGs tend to be star-formation-dominated in the MIR, $\sim 28\%$ – 50% host obscured AGN (Alexander et al. 2005, also see Figure 4) as predicted for the subset of mergers with initial conditions and orbits conducive to early (obscured) black hole growth. Furthermore, at least $\sim 30\%$ – 40% of luminous IRBGs have ULIRG-level SFRs (Tyler et al. 2009, this work). As rapid star formation is predicted throughout the obscured AGN phase of a major merger, this too is consistent with the major merger scenario.

This general picture is also supported by the work of Alexander et al. (2008a), Dey et al. (2008), and Brodwin et al. (2008). For instance, Alexander et al. (2008a) find that black hole growth in SMGs lags behind the growth of the host galaxy, contrary to what is seen in high-redshift optical (e.g., unobscured) and radio-selected samples of quasars (e.g., Peng et al. 2006; McLure et al. 2006). This finding suggests that SMGs are at an earlier evolutionary stage than their unobscured, AGN-dominated counterparts, again in agreement with the merger scenario. More generally, Dey et al. (2008) find that the surface densities and redshift distributions of $f_{24} \geq 300 \mu\text{Jy}$ IRBGs (at least $\sim 60\%$ of which are likely to be AGN-dominated in the MIR, Pope et al. 2008a) are comparable to those of luminous SMGs ($F_{850 \mu\text{m}} > 6 \text{ mJy}$, Chapman et al. 2005; Coppin et al. 2006). Similarly, Brodwin et al. (2008) analyze the clustering properties of IRBGs and find that $f_{24} \geq 300 \mu\text{Jy}$ IRBGs have

a correlation length comparable to that of SMGs (Blain et al. 2004). The most luminous ($f_{24} > 700 \mu\text{Jy}$) IRBGs, however, may be more strongly clustered, and thus lie in richer environments, than both their lower MIR-luminosity counterparts and the typical SMG.

While no one of these arguments confirms the potential merger origin for SMGs or IRBGs, collectively, the results suggest that the merger scenario first proposed by Sanders et al. (1988) may provide an acceptable explanation for the properties of these two samples. Ideally, one might hope to either confirm or reject this hypothesis on the basis of the observed morphologies. Unfortunately, however, the morphological properties of these samples remain amongst their most uncertain characteristics. As discussed in Section 7.1, the asymmetry measure, commonly used as a merger indicator in the local universe, suffers at high redshift from surface brightness dimming, a $(1+z)^4$ effect, and is insensitive to intermediate merger stages in which the galaxies lie at large separations. When using this measure alone, Swinbank et al. (2010) therefore conclude that SMGs are no more likely to appear as mergers than a bolometrically less luminous sample of high redshift star-forming galaxies. Optical (e.g., *i*-band) measurements of this and other objective morphology indicators are also complicated by the fact that at $z \sim 2$, the observed-frame optical emission probes the rest-frame UV emission, which tends to be more strongly clumped. However, when morphologies of AGN-dominated IRBGs are measured at longer wavelengths, the contribution from the unresolved AGN emission, now less obscured, can likewise bias the results (Bussmann et al. 2009; Melbourne et al. 2009).

Prior studies of IRBG morphology have therefore turned to the fraction of multiple resolved components as a measure of ongoing mergers, and have found a rate of only $\sim 15\%$ for IRBGs (Bussmann et al. 2009; Melbourne et al. 2009), far lower than is seen in local and high redshift samples of ULIRGs. However, this measure too is biased, and will not identify sources in the latest stages of a merger. We therefore chose to combine the asymmetry and near-neighbor/multiple-component methods, and conclude that the majority of both SMGs and IRBGs are likely to be undergoing mergers. Furthermore, the smaller physical size of the IRBGs, a trend first noted by Bussmann et al. (2009) and confirmed in Section 7.1.2, suggests that they are likely in a later, more relaxed merger stage, a hypothesis also supported by the AGN and star-forming characteristics presented above. Clearly, however, one would like to confirm this finding using a far larger, deeper, and higher-resolution sample, one that will be provided by the upcoming Cosmic Assembly Near-IR Deep Extragalactic Legacy Survey (CANDELS) *Hubble* WFC3 NIR imaging survey of the GOODS, COSMOS, EGS, and UDS fields.

9. SUMMARY

In summary, we present the X-ray, star-forming, and morphological properties of a sample of luminous ($f_{24} \gtrsim 700 \mu\text{Jy}$) IR-bright/optically-faint galaxies (IRBGs, $f_{24}/f_{\text{R}} \gtrsim 1000$) selected in deep X-ray fields. Our major findings are as follows.

1. The infrared colors and IRS spectra confirm that all of the $f_{24} \gtrsim 700 \mu\text{Jy}$ IRBGs are AGN dominated.
2. All of the sources appear to be X-ray obscured, and four remain X-ray non-detected despite deep X-ray coverage. As many as $\sim 40\%$ are strong Compton-thick candidates, and $\sim 40\%$ more appear to lie near the Compton-thick/heavily obscured ($N_{\text{H}} = 10^{24} \text{ cm}^{-2}$) boundary.

3. The mean intrinsic X-ray luminosity of the sample is $\log L_{0.5-8}(\text{erg s}^{-1}) \sim 44.6 \pm 0.4$, and all but one source has a MIR-derived intrinsic X-ray luminosity in excess of $\log L_{0.5-8}(\text{erg s}^{-1}) = 44$, the canonical dividing line between Seyfert galaxies and QSOs. These sources are therefore Type 2 QSOs from the X-ray perspective.
4. In general, the sources with the largest X-ray obscuration are those most likely to exhibit strong silicate absorption. Furthermore, at least two of the three IRBGs that are optically thick at $9.7 \mu\text{m}$ are likely to be undergoing mergers. However, silicate absorption need not accompany X-ray obscuration, and merger candidates are observed that lack strong silicate features.
5. 30%–40% of IRBGs have SFRs in the ULIRG range; presumably the rest of the sample also has relatively high levels of star formation that are masked by the AGN outputs.
6. As many as $\sim 70\%$ of the IRBGs in our sample show asymmetries indicative of mergers, similar to the incidence of mergers in SMGs at similar redshift. However, the IR-bright/optically-faint sources tend to be more compact than the SMGs, suggesting that they may be in a later stage of merging.
7. These characteristics are consistent with the proposal that these objects represent a later evolutionary stage following soon after the star-formation-dominated one represented by the SMGs.

J.L.D. thanks STScI for support through the Giacconi Fellowship, and Caltech/JPL for support through contract 1255094 to the University of Arizona, and D.M.A. thanks the Royal Society and Leverhulme Trust for a University Research Fellowship and Philip Leverhulme Prize, respectively. P. G. P.-G. acknowledges support from the Spanish Programa Nacional de Astronomía y Astrofísica under grants AYA 2006-02358 and AYA 2006-15698-C02-02, and from the Ramón y Cajal Program financed by the Spanish Government and the European Union. Finally, we thank Alex Pope, Elise Laird, Yong Shi, Jen Lotz, Laura Hainline, and the anonymous referee for helpful discussions and suggestions that improved the paper.

REFERENCES

- Alexander, D. M., Bauer, F. E., Chapman, S. C., Smail, I., Blain, A. W., Brandt, W. N., & Ivison, R. J. 2005, *ApJ*, 632, 736
- Alexander, D. M., et al. 2003, *AJ*, 126, 539
- Alexander, D. M., et al. 2008a, *AJ*, 135, 1968
- Alexander, D. M., et al. 2008b, *ApJ*, 687, 835
- Alonso-Herrero, A., et al. 2006, *ApJ*, 640, 167
- Arnouts, S., Vandame, B., Benoist, C., Groenewegen, M. A. T., da Costa, L., Schirmer, M., Mignani, R. P., & Slijkhuis, R. 2002, *VizieR Online Data Catalog*, 337, 90740
- Assef, R. J., et al. 2008, *ApJ*, 676, 286
- Barro, G., et al. 2010, *ApJS*, submitted
- Beswick, R. J., Muxlow, T. W. B., Thrall, H., Richards, A. M. S., & Garrington, S. T. 2008, *MNRAS*, 385, 1143
- Blain, A. W., Chapman, S. C., Smail, I., & Ivison, R. 2004, *ApJ*, 611, 725
- Boyle, B. J., Cornwell, T. J., Middelberg, E., Norris, R. P., Appleton, P. N., & Smail, I. 2007, *MNRAS*, 376, 1182
- Brand, K., et al. 2007, *ApJ*, 663, 204
- Brand, K., et al. 2008, *ApJ*, 680, 119
- Brodwin, M., et al. 2008, *ApJ*, 687, L65
- Buchanan, C. L., Gallimore, J. F., O’Dea, C. P., Baum, S. A., Axon, D. J., Robinson, A., Elitzur, M., & Elvis, M. 2006, *AJ*, 132, 401
- Bussmann, R. S., et al. 2009, *ApJ*, 693, 750
- Capak, P., et al. 2004, *AJ*, 127, 180
- Chapman, S. C., Blain, A. W., Smail, I., & Ivison, R. J. 2005, *ApJ*, 622, 772

- Conselice, C. J., Bershad, M. A., Dickinson, M., & Papovich, C. 2003a, *AJ*, **126**, 1183
- Conselice, C. J., Bershad, M. A., & Jangren, A. 2000, *ApJ*, **529**, 886
- Conselice, C. J., Blackburne, J. A., & Papovich, C. 2005, *ApJ*, **620**, 564
- Conselice, C. J., Chapman, S. C., & Windhorst, R. A. 2003b, *ApJ*, **596**, L5
- Coppin, K., et al. 2006, *MNRAS*, **372**, 1621
- Coppin, K., et al. 2010, *ApJ*, **713**, 503
- Cowie, L. L., Barger, A. J., Hu, E. M., Capak, P., & Songaila, A. 2004, *AJ*, **127**, 3137
- Dasyra, K. M., Yan, L., Helou, G., Surace, J., Sajina, A., & Colbert, J. 2008, *ApJ*, **680**, 232
- Davis, M., et al. 2007, *ApJ*, **660**, L1
- Desai, V., et al. 2009, *ApJ*, **700**, 1190
- Dey, A., et al. 2008, *ApJ*, **677**, 943
- Donley, J. L., Rieke, G. H., Pérez-González, P. G., & Barro, G. 2008, *ApJ*, **687**, 111
- Donley, J. L., Rieke, G. H., Pérez-González, P. G., Rigby, J. R., & Alonso-Herrero, A. 2007, *ApJ*, **660**, 167
- Donley, J. L., Rieke, G. H., Rigby, J. R., & Pérez-González, P. G. 2005, *ApJ*, **634**, 169
- Draine, B. T. 2003, *ARA&A*, **41**, 241
- Efstathiou, A., Hough, J. H., & Young, S. 1995, *MNRAS*, **277**, 1134
- Fadda, D., et al. 2010, *ApJ*, in press (arXiv:1006.2873)
- Farrah, D., et al. 2008, *ApJ*, **677**, 957
- Fiore, F., et al. 2008, *ApJ*, **672**, 94
- Fiore, F., et al. 2009, *ApJ*, **693**, 447
- Franceschini, A., et al. 2003, *MNRAS*, **343**, 1181
- Gendreau, K. C., et al. 1995, *PASJ*, **47**, L5
- Georgakakis, A., Rowan-Robinson, M., Nandra, K., Digby-North, J., Pérez-González, P. G., & Barro, G. 2010, *MNRAS*, **406**, 420
- Georgantopoulos, I., Akylas, A., Georgakakis, A., & Rowan-Robinson, M. 2009, *A&A*, **507**, 747
- Georgantopoulos, I., Georgakakis, A., Rowan-Robinson, M., & Rovilos, E. 2008, *A&A*, **484**, 671
- George, I. M., Turner, T. J., Yaqoob, T., Netzer, H., Laor, A., Mushotzky, R. F., Nandra, K., & Takahashi, T. 2000, *ApJ*, **531**, 52
- Gialalisco, M., et al. 2004, *ApJ*, **600**, L93
- Hainline, L. J., Blain, A. W., Smail, I., Frayer, D. T., Chapman, S. C., Ivison, R. J., & Alexander, D. M. 2009, *ApJ*, **699**, 1610
- Heckman, T. M. 1995, *ApJ*, **446**, 101
- Hickox, R. C., & Markevitch, M. 2006, *ApJ*, **645**, 95
- Hopkins, P. F., Hernquist, L., Cox, T. J., & Kereš, D. 2008, *ApJS*, **175**, 356
- Houck, J. R., et al. 2004, *ApJS*, **154**, 18
- Houck, J. R., et al. 2005, *ApJ*, **622**, L105
- Ibar, E., et al. 2008, *MNRAS*, **386**, 953
- Ivison, R. J., et al. 2007, *ApJ*, **660**, L77
- Kellermann, K. I., Fomalont, E. B., Mainieri, V., Padovani, P., Rosati, P., Shaver, P., Tozzi, P., & Miller, N. 2008, *ApJS*, **179**, 71
- Laird, E. S., et al. 2009, *ApJS*, **180**, 102
- Lanzuisi, G., Piconcelli, E., Fiore, F., Feruglio, C., Vignali, C., Salvato, M., & Gruppioni, C. 2009, *A&A*, **498**, 67
- Le Fèvre, O., et al. 2004, *A&A*, **417**, 839
- Lehmer, B. D., et al. 2005, *ApJS*, **161**, 21
- Lotz, J. M., Jonsson, P., Cox, T. J., & Primack, J. R. 2008, *MNRAS*, **391**, 1137
- Luo, B., et al. 2008, *ApJS*, **179**, 19
- Lutz, D., Maiolino, R., Spoon, H. W. W., & Moorwood, A. F. M. 2004, *A&A*, **418**, 465
- Maiolino, R., Shemmer, O., Imanishi, M., Netzer, H., Oliva, E., Lutz, D., & Sturm, E. 2007, *A&A*, **468**, 979
- Marshall, F. E., Boldt, E. A., Holt, S. S., Miller, R. B., Mushotzky, R. F., Rose, L. A., Rothschild, R. E., & Serlemitsos, P. J. 1980, *ApJ*, **235**, 4
- Marzke, R., et al. 1999, in ASP. Conf. Ser. 191, Photometric Redshifts and the Detection of High Redshift Galaxies, ed. R. Weymann, L. Storrie-Lombardi, M. Sawicki, & R. Brunner (San Francisco, CA: ASP), 148c
- Mason, R. E., Geballe, T. R., Packham, C., Levenson, N. A., Elitzur, M., Fisher, R. S., & Perlman, E. 2006, *ApJ*, **640**, 612
- McLure, R. J., Jarvis, M. J., Targett, T. A., Dunlop, J. S., & Best, P. N. 2006, *MNRAS*, **368**, 1395
- Melbourne, J., et al. 2009, *AJ*, **137**, 4854
- Menéndez-Delmestre, K., et al. 2009, *ApJ*, **699**, 667
- Murphy, E. J., Chary, R., Alexander, D. M., Dickinson, M., Magnelli, B., Morrison, G., Pope, A., & Teplitz, H. I. 2009, *ApJ*, **698**, 1380
- Narayanan, D., Hayward, C. C., Cox, T. J., Hernquist, L., Jonsson, P., Younger, J. D., & Groves, B. 2010a, *MNRAS*, **401**, 1613
- Narayanan, D., et al. 2010b, *MNRAS*, in press (arXiv:0910.2234)
- Papovich, C., et al. 2007, *ApJ*, **668**, 45
- Peng, C. Y., Impey, C. D., Rix, H., Kochanek, C. S., Keeton, C. R., Falco, E. E., Lehár, J., & McLeod, B. A. 2006, *ApJ*, **649**, 616
- Pérez-González, P. G., et al. 2005, *ApJ*, **630**, 82
- Pérez-González, P. G., et al. 2008, *ApJ*, **675**, 234
- Perola, G. C., et al. 2004, *A&A*, **421**, 491
- Pier, E. A., & Krolik, J. H. 1992, *ApJ*, **401**, 99
- Polletta, M., Weedman, D., Hönig, S., Lonsdale, C. J., Smith, H. E., & Houck, J. 2008, *ApJ*, **675**, 960
- Polletta, M. d. C., et al. 2006, *ApJ*, **642**, 673
- Pope, A., Borys, C., Scott, D., Conselice, C., Dickinson, M., & Mobasher, B. 2005, *MNRAS*, **358**, 149
- Pope, A., et al. 2006, *MNRAS*, **370**, 1185
- Pope, A., et al. 2008a, *ApJ*, **689**, 127
- Pope, A., et al. 2008b, *ApJ*, **675**, 1171
- Ptak, A., Heckman, T., Levenson, N. A., Weaver, K., & Strickland, D. 2003, *ApJ*, **592**, 782
- Richards, E. A. 2000, *ApJ*, **533**, 611
- Rieke, G. H., Alonso-Herrero, A., Weiner, B. J., Pérez-González, P. G., Blaylock, M., Donley, J. L., & Marcillac, D. 2009, *ApJ*, **692**, 556
- Rigby, J. R., et al. 2008, *ApJ*, **675**, 262
- Sajina, A., Yan, L., Armus, L., Choi, P., Fadda, D., Helou, G., & Spoon, H. 2007, *ApJ*, **664**, 713
- Sajina, A., et al. 2008, *ApJ*, **683**, 659
- Sanders, D. B., Soifer, B. T., Elias, J. H., Madore, B. F., Matthews, K., Neugebauer, G., & Scoville, N. Z. 1988, *ApJ*, **325**, 74
- Shi, Y., Rieke, G., Lotz, J., & Perez-Gonzalez, P. G. 2009, *ApJ*, **697**, 1764
- Shi, Y., et al. 2006, *ApJ*, **653**, 127
- Sturm, E., Hasinger, G., Lehmann, I., Mainieri, V., Genzel, R., Lehnert, M. D., Lutz, D., & Tacconi, L. J. 2006, *ApJ*, **642**, 81
- Sturm, E., et al. 2005, *ApJ*, **629**, L21
- Swinbank, A. M., Smail, I., Chapman, S. C., Blain, A. W., Ivison, R. J., & Keel, W. C. 2004, *ApJ*, **617**, 64
- Swinbank, A. M., et al. 2010, *MNRAS*, in press (arXiv: 1002.2518)
- Szokoly, G. P., et al. 2004, *ApJS*, **155**, 271
- Teng, S. H., Wilson, A. S., Veilleux, S., Young, A. J., Sanders, D. B., & Nagar, N. M. 2005, *ApJ*, **633**, 664
- Treister, E., et al. 2009, *ApJ*, **706**, 535
- Tyler, K. D., et al. 2009, *ApJ*, **691**, 1846
- Vandame, B., et al. 2001, arXiv:astro-ph/0102300
- Veilleux, S., et al. 2009, *ApJS*, **182**, 628
- Villar, V., Gallego, J., Pérez-González, P. G., Pascual, S., Noeske, K., Koo, D. C., Barro, G., & Zamorano, J. 2008, *ApJ*, **677**, 169
- Weedman, D. W., Le Floch, E., Higdon, S. J. U., Higdon, J. L., & Houck, J. R. 2006a, *ApJ*, **638**, 613
- Weedman, D. W., et al. 2006b, *ApJ*, **651**, 101
- Werner, M. W., et al. 2004, *ApJS*, **154**, 1
- Wolf, C., et al. 2004, *A&A*, **421**, 913
- Yan, L., et al. 2005, *ApJ*, **628**, 604